ORIGINAL RESEARCH ARTICLE

Existence and Significance of Local Overheating in Spark Plasma Sintered NiAl: Experimental and Numerical Investigation

FATIMA NISAR, MACIEJ ZIĘTARA, ADAM KRUK, PIOTR JENCZYK, SZYMON NOSEWICZ, KAMIL KASZYCA, MARCIN CHMIELEWSKI, and JERZY ROJEK

This work presents a combined experimental and numerical investigation of local overheating in NiAl during spark plasma sintering (SPS). Experimental studies were conducted on samples sintered under different temperature and pressure conditions to capture both the early and final stages of densification. Both perpendicular and parallel loading directions were analysed for microstructural evidence of local melting. Experimental research comprised post-process analysis using SEM and EBSD, while supplementary XRD analysis was used to assess phase stability and crystallographic characteristics. Microstructural analysis focused on regions most susceptible to overheating (contact areas, small particles trapped between larger ones). Sintered samples showed progressive densification, neck growth and grain coarsening with increasing temperature. EBSD maps of sintered compacts reveal distinct orientations across contacts, with no evidence of epitaxial or equiaxed grain growth. Experimentally, no evidence of melting due to local overheating was detected. The experimental observations were complemented by particle-scale thermo-electric FEM simulations. Geometries of equal-sized particles, arranged in a straight line and in a zig-zag chain, connected by the necks with increased resistance, were considered to analyse the temperature rise in the necks. Geometry consisting of a small particle between two large particles was analysed to assess temperature nonuniformity in heterogeneous microstructures. The results show temperature increase in contacts or in small particles; however, the resulting temperature differences are less than 1 °C in all cases studied. Numerical results support the experimental findings that NiAl is not prone to local overheating in SPS under the studied conditions.

https://doi.org/10.1007/s11661-026-08328-3

I. INTRODUCTION

SPARK plasma sintering (SPS), also referred to as field-assisted sintering technology (FAST), has become a widely used technique for rapid consolidation of metals,[1] ceramics, semi-conductors[2] and composites.[3,4] Its efficiency is generally attributed to the simultaneous application of uniaxial pressure and electric current, which enables rapid heating rates, short dwell times, and high density levels at comparatively lower temperatures than conventional sintering methods.[5–8]

SPS couples thermal, electrical and mechanical effects at multi-scales. The flow of electric current through a network of particle contacts results in a nonuniform current density at the particle level, producing nonuniform Joule heating that can lead to local overheating.[9] Electric current is concentrated at particle contacts and necks; therefore, local overheating may occur in this area. In addition to contact-scale hotspots, particle size itself may influence local thermal response. Specific Joule heating is higher in smaller particles.[10]

Different studies attribute SPS benefits to local increase in temperature resulting micro-hotspots, which can accelerate bonding and promotes neck formation and neck growth at lower temperatures.[11] However, excessive local overheating may produce local melting, uncontrolled grain growth,[12] phase transformation[13]

The handling Editor for this article was Jonathan Cormier.

FATIMA NISAR, PIOTR JENCZYK, SZYMON NOSEWICZ, and JERZY ROJEK are with the Institute of Fundamental Technological Research, Polish Academy of Sciences, Pawińskiego 5B, 02-106 Warsaw, Poland. Contact e-mail: fnisar@ippt.pan.pl MACIEJ ZIĘTARA and ADAM KRUK are with the AGH University of Krakow, al. Adama Mickiewicza 30, 30-059 Kraków, Poland. KAMIL KASZYCA and MARCIN CHMIELEWSKI are with the Łukasiewicz – Institute of Microelectronics and Photonics, 12 Wólczyńska 133, 01-919 Warsaw, Poland.
Manuscript submitted April 1, 2026; accepted July 20, 2026.

Published online: 20 August 2026

or segregation, and non-uniform microstructural development[5]—outcomes that undermine the principal advantages of SPS by producing microstructural inhomogeneity and hence non-uniform material properties. Whether such local overheating is significant in conductive intermetallics remains unresolved.[5,14] In this work, we combine experimental observations and particle-scale numerical modelling in NiAl to determine the existence and microstructural significance of local overheating in SPS.

Nickel aluminide (NiAl) is a particularly attractive high-temperature, low-density intermetallic, combining high thermal conductivity, excellent oxidation resistance and the ability to retain strength and stiffness at elevated temperatures, which has driven continuous interest for advanced aerospace and energy applications.[15–18] Extensive investigations of its mechanical and physical properties have consequently led to numerous proposed structural and non-structural uses, including jet-engine components, stationary gas–turbine systems for power generation, internal combustion engines and high-temperature heat exchangers.[15] Notably, Darolia[19] demonstrated the technological potential of NiAl by evaluating several NiAl-based alloys as turbine engine blades, vanes and combustor shingles, highlighting both the promise and the processing challenges of this intermetallic in demanding service environments. Historically, NiAl has been produced by casting, rapid solidification or powder-based routes, but casting is costly for intermetallics with high melting points, and conventional sintering faces challenges such as persistent surface oxides on aluminium that inhibit full densification.[20,21] Consequently, SPS strategies (reactive SPS or combined mechanical-alloying with SPS) have been adopted to overcome these limitations by promoting faster consolidation, aiding oxide removal and enabling reactive synthesis of the intermetallic phase.[21,22] However, to reliably exploit SPS for NiAl it is essential to clarify the underlying sintering mechanisms in the presence of an applied current.

The existence and role of local overheating due to Joule effect or plasma formation during spark plasma sintering remain a contested topic in the literature. While early hypotheses claimed microscopic plasma discharges between powder particles cause exceptionally fast sintering and anomalous microstructures,[23] more recent reviews stress that unequivocal proof of plasma formation under typical SPS conditions is lacking.[6,24] Saunders *et al.*[25] used *in situ* atomic emission spectroscopy to show that plasma emission was not detected under conventional SPS voltages (below 10 V) and typical pressures, although plasma could be observed in pressureless experiments at much higher voltages (above 50 V) and when the graphite die was removed to force all current through the powder bed. Marder *et al.*[26] studied densification of LiF in SPS conditions and showed that low pressure (2 MPa) and low temperature (500 °C) resulted in plasma formation. Similarly, in another article Marder *et al.*[27] studied YAG nanopowders and observed rod-like material jets bridging particle gaps, which they interpreted as evidence of liquid formation and plasma-assisted surface softening during densification. But at the same time, it was discussed that such features were limited to particular conditions and were absent once the microstructure became more connected and dense. In ceramics, low conductivity allows limited electric current through the powder and a gap in the microstructure obstructs the current, causing charge build-up and hence surface discharge. However, in metallic materials, high conductivity allows both current and heat to diffuse rapidly, limiting local overheating and making plasma formation far less probable. In short, plasma generation is a localised, process-dependent phenomenon that may occur only in specific materials and under certain SPS conditions, rather than a universal feature of SPS.

A large amount of experimental and theoretical work has focused on the assessment of Joule heating concentration at inter-particle contacts and its consequences for material processing and properties. Direct, *in situ* measurement of temperature at the individual-particle level during an SPS process is generally not feasible, although some attempts have been made to directly observe idealised particle systems under SPS conditions using specialised laboratory setups.[28–30] Kudryashov *et al.*[28] have built an experimental apparatus to replicate SPS key mechanisms. The system enables direct visualisation of powder particle chains located within the channels of a dielectric matrix during the application of short electrical current pulses. Using this apparatus, Rogachev *et al.*[29] conducted experiments on chains of spherical titanium particles of diameter 300 μm, revealing pronounced overheating at the contact points and liquid-phase sintering necks when a short ($\sim$ 1 ms) current pulse was applied.

Trapp and Kieback[30] investigated inhomogeneous temperature distribution in copper and martensitic steel spheres for the initial stage of FAST/SPS using capacitor discharges applied to three to ten 1 mm diameter spheres, placed in a glass tube. They estimated the temperature at the contacts under extreme conditions using melting of particle coatings as a temperature indicator. They extrapolated these results to the much lower currents typical of real SPS to estimate local overheating at particle contacts and concluded that the local temperature increase at particle contacts is very small—on the order of 0.05 K to 5 K even under strong electrical loading. Yanagisawa *et al.*[31] investigated the response of uniformly sized relatively large (mean diameter approximately 550 μm) spherical copper powder particles within a compact during a single 500 ms electrical discharge, using optical microscopy for in situ observation. The experiment involved roughly 250 particles. Their observations indicated that neck formation occurred through melting, driven by elevated temperatures generated locally at particle contact points. Estimates of Joule heating suggested that very high temperatures could develop at the interparticle contacts during the early stage of compaction. However, the thermal analysis assumed adiabatic conditions, *i.e.*, heat transfer by conduction was neglected. Hu *et al.*[14] emphasise that the sample resistance during the early stages of consolidation is dominated by contact resistances because of oxide films and imperfect contacts;

therefore, the majority of Joule heating initially originates at particle–particle contacts. As densification proceeds and contacts grow, this contact contribution falls off.[32] Ghosh *et al.*[33] similarly pointed out that electrical (or Kapitza-type) resistance at interfaces concentrates ohmic heating at boundaries, which can promote a local increase in temperature.

The review of multi-physical fields induced phenomena and effects in spark plasma sintering by Hu *et al.*[14] includes a number of works on heat localisation in various applications. Most of the research on local overheating during an SPS process relied on post-process microstructural evidence, sometimes combined with numerical modelling to infer whether solid-state phase change or melting and re-solidification occurred at contacts. Bernardo *et al.*[34] investigated the effect of different electrical conditions on the microstructure of bulk $BiFeO_3$ and Ti-doped $BiFeO_3$. Their findings showed that sintering under direct current can produce non-uniform microstructures arising from localised current flow and the development of internal thermal gradients within the samples. Zuniga *et al.*[35] investigated Spark Plasma Sintering of a nanocrystalline Al–Cu–Mg–Fe–Ni–Sc alloy. The microstructure observed after SPS processing consisted of coarse-grained regions and fine-grained regions ($\sim$ 1 μm and $\sim$ 150 nm, respectively). The formation of coarse grains was explained by localised heating at grain boundaries.

Recent work on Nd–Fe–B sintering by Tomše *et al.*[36] reported an emergent phase at temperatures well below its equilibrium transformation, suggesting anomalies that may signal local Joule heating. In another study,[37] the authors sintered TiAl using SPS and reported the formation of an unexpected phase due to the breakdown of a highly resistive surface contamination layer of oxides. However, it was just microstructural inhomogeneity and no change in XRD patterns was observed as compared to the as-received powder.

The above-reviewed experimental works report local melting for special conditions, such as relatively large (hundreds of micrometres to one millimetre) particles subjected to intense, short current pulses. Analytical models predicting extremely large, even thousands-of-degrees temperature rises were based on adiabatic assumptions neglecting conductive heat dissipation.[11,31] Several authors therefore cautioned that models assuming no heat conduction within particles can dramatically overestimate contact temperature rises, and that observed fine grains at necks can also result from severe plastic deformation and recrystallisation rather than melting.[11,38]

On the other hand, various experimental studies and improved multiphysics simulations that account for heat conduction within micron-scale particles tend to find much smaller contact temperature elevations. Collard *et al.*[38] and Trzaska *et al.*[39] searched for phase transformations in sintered TiAl prepared from starting powder with a diameter of 100 μm, but found no evidence of overheating-induced phase change. FEM simulations were used to show that, although current density concentrates at inter-particle necks, rapid heat conduction keeps the temperature difference between the neck and the particle centre below 1 °C.

Trapp *et al.*[40] performed analytical and numerical two-sphere studies and concluded that for particle sizes below about 1 mm local overheating is below 1 K and that pulsing the current has negligible influence on the densification rate, implying that classical pressure and curvature driven mechanisms dominate under typical SPS conditions. Trzaska and Monchoux[41] examined an electromigration-sensitive Ag–Zn reactive system and found that the intermetallic layer width was essentially identical for current-insulated and high current-density experiments, suggesting that, at least in some reactive systems, current density does not noticeably alter reaction extent.

Microscopic modelling efforts have diverged in scope and conclusion as well. Simplified adiabatic analytical treatments and capacitor-discharge experiments can predict very high, short-lived contact temperatures (and have demonstrated arcs under extreme conditions).citeYanagisawasps2003,Songsps2006 In contrast, multiphysics FEM and analytical two-sphere models that incorporate realistic heat conduction, contact geometry, material thermophysical properties and typical SPS voltages/pressures generally predict only small, rapidly dissipated temperature differences between necks and particle centres for micron-scale powders.[38,40]

The literature review herein shows the importance of NiAl sintered using SPS and shows the significance of analysing material-specific behaviour of NiAl during sintering. Non-uniform electric current in SPS due to non-uniformity in resistivity may cause a local increase in temperature due to the Joule effect. The objective of this work is to investigate the presence of local overheating during SPS of NiAl and to assess its implications for microstructure evolution. The present study combines post-processing microstructural examination with multiphysics analysis to evaluate contact-scale temperature increase under typical SPS conditions.

Unlike previous works, which were mainly focused on overheating at the contacts between equal-sized particles,[38–40] this study investigates both contact areas and regions with strong heterogeneity in particle size, *i.e.*, places where small particles are surrounded by large ones. Therefore, we examine the post-sintering microstructure paying particular attention to such areas that are more prone to overheating. Numerically, we investigate local overheating in geometries with equal-sized particles, as well as in a heterogeneous geometry where a small particle is in contact with two large particles. Multiphysics simulations go beyond adiabatic[11,31] and ideal-neck simplifications[38] by including heat conduction within particles and accounting for imperfect contacts that affect local Joule heating and heat flow between particles.

The paper is organised as follows. Section II presents the methodology, including manufacturing process and characterisation techniques. Section III discusses the resulting observations from experimental work. Section IV presents the numerical analysis. Finally, Section V summarises the main findings. Supplementary

material for the experimental and numerical analysis is presented in "Appendices".

II. METHODOLOGY

A. *Initial Powder Characterization*

For sintering, we used gas-atomised spherical NiAl powder from Goodfellow with a purity of 99.9 pct. Figure 1 shows spherical morphology of the NiAl powder. Particle size distribution, illustrated in Figure 2, was determined using the Clemex image analysis system. Particle size distribution is characterised by a weighted volume average of 12.27 μm and a median of 9.25 μm. Although particle size approximately range from 1 to 100 μm, 90 pct of the volume is occupied by particles of diameter less than 23 μm.

B. *Spark Plasma Sintering Process*

Sintering was carried out on an FCT—HHP D25 SPS apparatus. at Fraunhofer Institute for Ceramic Technologies and Systems IKTS. Powder charges of approximately 25 g were placed in a graphite die (SGL R7710) of inner and outer diameters of 30 and 50 mm, respectively. Two layers of graphite foil (grade TH) of thickness 0.25 mm were used to separate powder from the tooling and to improve thermal and electrical conductivity of the contacts. Tooling was thermally insulated with a graphite felt (GFA10) of thickness 10 mm. The assembled tooling with powder was then placed in the furnace, and a uniaxial pressure of 30 MPa was applied. A continuous DC current was applied (low voltage high current mode). Samples were heated at a rate of 100 °C/min to different sintering temperatures and held for 5 minutes while maintaining the pressure. After the heating and dwell time, samples were unloaded and cooled at 100 °C/min simultaneously. The process was performed under a vacuum of approximately 0.1 mbar. Figure 3 shows the temperature ramp, dwell time and cooling of the SPS cycle together with the applied pressure for one of the samples as an example.

It should be noted that one of the samples was partially melted as a reference. This reference sample was heated to 1620 °C to produce visible melt-related microstructures that can be used as a diagnostic reference when interpreting the sintered samples. The microstructural analysis of this partially melted sample is provided in "Appendix A". By comparing microscopic signatures from this melted-reference sample with the sintered samples, we can identify which features are associated with melting and resolidification.

The samples were sintered at low and high temperatures ranging from 700 °C to 1550 °C. In literature, typical solid-state sintering of NiAl is performed at temperatures well below the melting point of 1650 °C.[42] Commonly reported sintering temperatures for NiAl range from 1100 °C to 1400 °C.[43] In order to maximise the chances of observing any contact-scale overheating during SPS, we selected sintering temperatures in a broad range, particularly at higher temperatures.

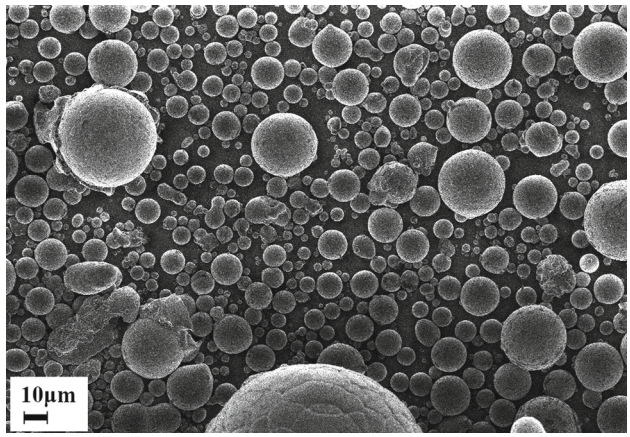

Fig. 1—NiAl powder morphology.

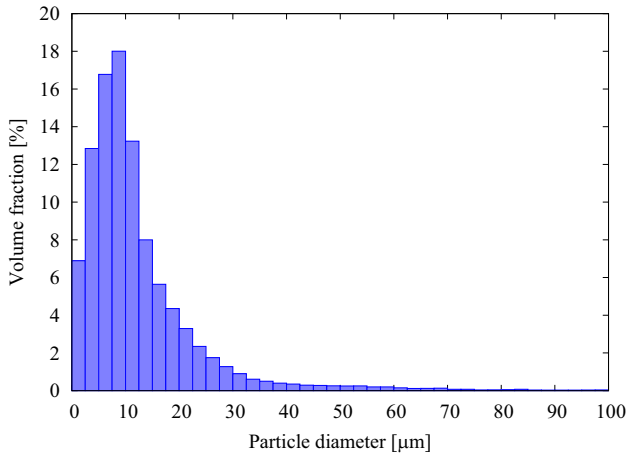

Fig. 2—NiAl powder particle size distribution.

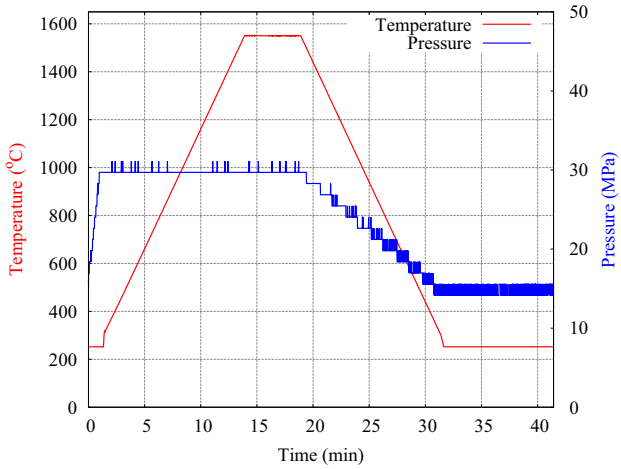

Fig. 3—Temperature and pressure profile for Sample 5 sintered at 1550 °C.

Table I gives all the processing conditions. All samples were processed in the same SPS setup and with identical tooling, graphite foil/felt and pressure. Only

Table I. SPS Sintering Processing Parameters and Density

	Temperature (°C)	Pressure (MPa)	Density ρ_{rel} (Pct)
Sample 1	700	5	—
Sample 2	1100	5	70.2
Sample 3	1350	30	93.3
Sample 4	1450	30	97.7
Sample 5	1550	30	99.6

the prescribed sintering temperature and pressure was varied.

After sintering, the compacts were sectioned for microstructural characterisation by standard metallographic techniques. Bulk density ρ_b, being an indicator of sintering, was measured by Archimedes' method following ASTM B962.[44] The relative densities of the samples with respect to processing parameters are shown in Table I. The relative density $\rho_{rel} = \rho_b/\rho_0$ was calculated by taking the density of fully compact NiAl ($\rho_0 = 5910$ kg/m^3).

C. *Characterisation Techniques Used to Detect Local Melting*

This section outlines the methods used to characterise sintered NiAl and to identify signatures of partial melting. For each technique, we first specify acquisition parameters (magnification, step size, detectors, beam energy, *etc.*), then describe the microstructural and crystallographic features that would indicate melting or resolidification (*e.g.*, melt pools, epitaxial regrowth, bimodal grain-size distributions).

1. *Sample preparation for microscopic analysis*

Samples were metallographically prepared by conventional grinding and polishing. Grinding was carried out with SiC sandpapers (grade: 360, 600 and 1000). Polishing was done using successive diamond suspensions of 9, 3 and 1 μm followed by chemical–mechanical polish using OP-S (Si suspension of 0.25 μm) to produce a defect-free surface. Finally, the samples were cleaned ultrasonically in ethanol prior to microstructural characterisation.

2. *SEM imaging: parameters and melting indicators*

Microstructure was analysed using a high-resolution scanning electron microscope (SEM) Merlin Gemini II (ZEISS), equipped with a field emission gun (FEG).

The SEM images were acquired using an accelerating voltage of 15 kV with a BSE (AsB) detector.

In SEM images, localised partial melting can be identified as fluid-like features: thin wetting layer bridging particles, resolidified pools at triple junctions or irregular necks. For example, some studies combining SPS with prior ball milling report microstructural evidence of the formation of melt at the inter-particle contacts (*i.e.*, tiny pools of liquid and irregular necks) in mixed-powder composites.[45,46] Such morphologies contrast with the faceted or sintered-neck geometries produced by solid-state diffusion and grain-boundary migration. These liquid-phase signatures are well-documented in liquid-phase sintering and in SPS studies of eutectic or multiphase systems where local melting is expected.[13,47,48]

3. *EBSD mapping: parameters and melting indicators*

Crystallographic analysis was performed using an EBSD detector (Bruker Quantax CrystAlign 400) mounted on a scanning electron microscope operated at an accelerating voltage of 20 kV with a specimen tilt of 70 deg. EBSD maps were acquired at two spatial resolutions corresponding to low- and high-resolution scans. Low-resolution maps (used for grain size statistics) were collected with a step size of 3.9 μm, while high-resolution maps (used for detailed analysis of particle contacts and local microstructural features) were acquired with a step size of 0.78 μm. The step size was selected to ensure adequate spatial resolution relative to the observed grain size.

Additionally, scans at higher magnification were performed with a step size of 0.4 μm. The 0.4 μm scans produced the same crystallographic interpretation as the 0.78 μm scans, with no evidence of epitaxial growth, orientation inheritance, or fine equiaxed grains indicative of resolidification. Therefore, the step size of 0.78 μm was considered adequate for the analysis presented in this study. Grains were defined using a critical misorientation angle of 15 deg, and grains smaller than 3 pixels were excluded from the analysis.

EBSD mapping provides direct crystallographic evidence useful for identifying local melting and subsequent resolidification.[13] Epitaxial resolidification can be identified in EBSD maps when a thin region melts and resolidifies by lateral growth from a neighbouring grain; the resolidified area may retain the same crystallographic orientation. Such orientation continuity (or strong local texture) is commonly reported in remelting/solidification studies, including laser and additive manufacturing processes.[49] Another possible mechanism is independent solidification or recrystallisation. If a region melts and subsequently nucleates upon cooling, the resolidified area typically contains fine equiaxed grains with orientations that are random relative to neighbouring grains, producing a local population of small grains.[50] This results in a bimodal grain size distribution. In both cases—epitaxial solidification or independent recrystallisation—EBSD maps are expected to show either orientation inheritance or localised clusters of newly formed, randomly oriented fine grains. The absence of such features is therefore interpreted as lack of clear microstructural evidence of local melting.

III. RESULTS AND DISCUSSION

Herein the microstructure at different stages of sintering is studied and compared to analyse local overheating in spark plasma sintering. Effect of loading direction on microstructure is also studied for the samples sintered at higher pressure.

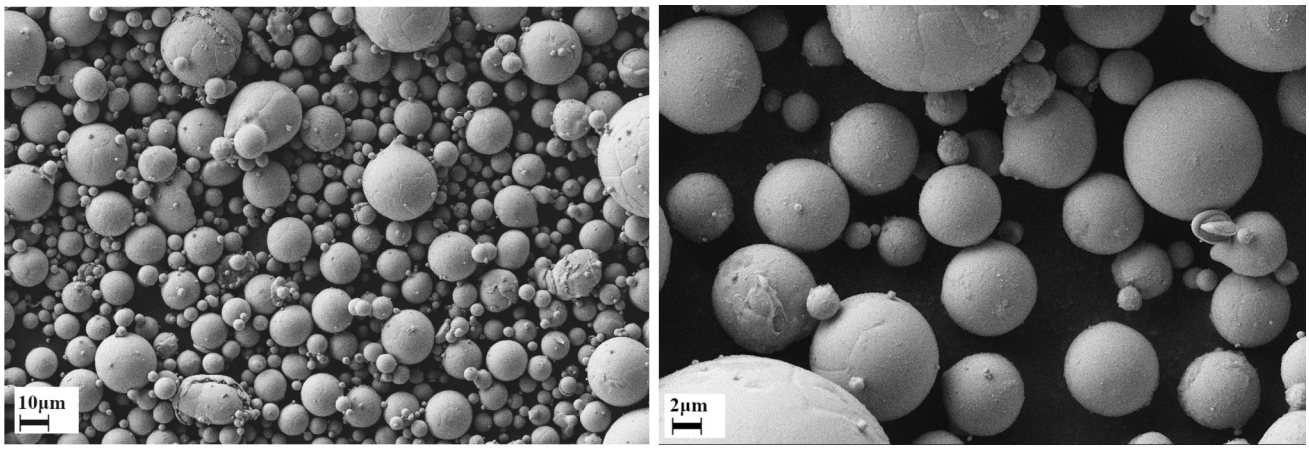

Fig. 4—SEM images of powder from the Sample 1 sintered at 700 °C: (*a*) low magnification, (*b*) high magnification.

A. *Low Temperature and Low Pressure Sintering*

To obtain evidence of possible local melting at lower temperatures, NiAl was heated till 700 °C. The compact was weakly bonded and easily disintegrated into loose powder. Figure 4 presents SEM images of powder obtained after de-agglomerating the partially sintered compact. Predominantly spherical particle morphology can be seen with a few weak interparticle bonds, suggesting early-stage solid-state bonding rather than melting and wetting which would have resulted in fused necks.

Additionally, another sample was sintered at 1100 °C to analyse the intermediate stage of sintering. Figures 5(a) and (b) show low and high magnification SEM images of the sample sintered at 1100 °C. The cross-section presented is parallel to the loading direction. The images indicate that the powder compact retains much of its original particle morphology, with spherical particles clearly visible and only limited neck formation at the contact points. Some particles appear slightly flattened at the grain-boundary, suggesting the onset of thermal softening and densification, but no melt-like features, flow traces, or resolidified pools are observed. The EBSD IPF orientation map for Z-direction in Figure 5(c) confirms that the microstructure consists of distinct crystallographic orientations with clear boundaries between them. At low sintering temperature, subgrains within large particles are visible.

B. *High Temperature and High Pressure Sintering*

Figures 6 and 7 present SEM images of the cross-sections of samples sintered at 1350 °C, 1450 °C and 1550 °C, taken in both the perpendicular and parallel loading directions. In general, the two orientations reveal the same microstructural evolution, with only minor differences in particle shape. A slight particle deformation due to compression can be seen in the parallel direction, which is consistent with the uniaxial loading, but no melting or abnormal neck formation is observed.

Low-magnification images (Figure 6) show an overall microstructural evolution, whereas higher-magnification images (Figure 7) reveal neck growth and grain-boundary development. A gradual evolution in morphology is observed as sintering temperature increases. At 1350 °C (Figures 6(a) and (b)), the compact exhibits well-defined particle outlines and mainly spherical particle surfaces; small necks and porosity are visible. At 1450 °C (Figures 6(c) and (d)), necks grow significantly and contact areas increase, while reducing the overall free surface area of the particles and pores. At 1550 °C (Figures 6(e) and (f)), the particle outlines are less spherical, and grains appear irregular and more coalesced; neck regions grow further, and many grains show faceted morphologies. Moreover, it can be observed that with increasing sintering temperature, the subgrain boundaries annihilate. This process is commonly observed at high temperatures where thermal energy accelerates atomic diffusion, driving the annihilation of low-angle subgrain boundaries.[51]

At higher magnification (Figure 7), grain boundaries and particles' morphology are more clearly visible. It can be observed that large equal-sized particles form flat grain boundaries, whereas in the case of unequal-sized particles, smaller particles are indented into the surfaces of larger neighbouring particles. This is in agreement with the deformation behaviour of elasto-plastic spheres with a large difference in sizes.[52] The local deformation associated with indentation is more visible at higher temperatures. Additionally, at 1550 °C (Figures 7(e) and (f)), we can also see the irregular shape of grains due to bulk deformation of particles at temperatures close to the melting point as the yield stress decreases.

From these observations, it is evident that spherical particle morphology persists in the initial stages of sintering when the densification is mainly due to diffusional creep. In the later stages of sintering, when the temperature is higher (close to the melting point), yield stress decreases, and plastic deformation causes particles to coalesce into irregular, faceted grains.

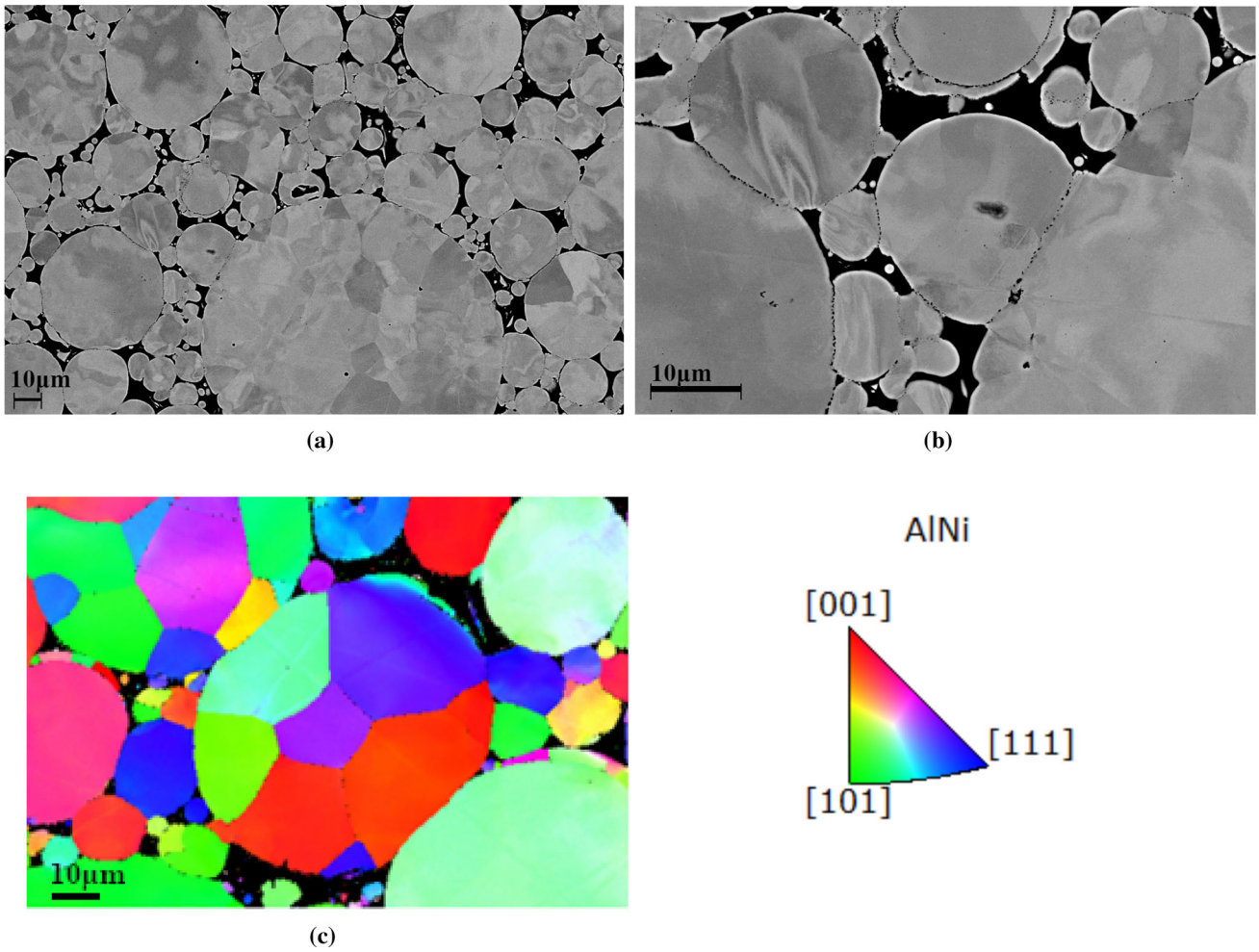

Fig. 5—Sample 2 sintered at 1100 °C (cross-section parallel to loading direction): (*a*, *b*) SEM images, and (*c*) EBSD map.

It is important to note that none of the sintered samples exhibits topological evidence of local melting (*e.g.*, liquid-like flow features or pooled material), which are visible only in the melted reference sample.

Figures 8 and 10 present low and high resolution EBSD IPF-Z maps of the samples sintered at 1350 °C, 1450 °C and 1550 °C in both perpendicular and parallel loading directions. Cross-sections from both orientations at low magnification with a step size of 3.9 μm in Figure 8 exhibit grains with a largely random distribution of orientations. Distinct crystallographic orientations are observed across particle contacts, and no clear evidence of orientation inheritance that would indicate epitaxial resolidification is detected. Furthermore, no localised clusters of fine, randomly oriented equiaxed grains are observed that could be associated with melting followed by independent nucleation. Overall, the perpendicular and parallel EBSD maps support the same conclusion—the microstructure evolves mainly through densification, without any evidence of contact-scale melting in either cross-section.

The grain size histograms in Figure 9, based on number fraction, quantify the progressive coarsening of grains observed in the microstructure. At 1350 °C, the microstructure consists of spherical grains with a volume average D_{50} grain size of approximately 13.02 μm. Increasing the sintering temperature to 1450 °C results in noticeable microstructural coarsening, with the average grain size increasing to 19.08 μm. At 1550 °C, grain growth becomes more pronounced, and the average grain size further increases to 27.97 μm. All the distributions (shown in Figure 9) are unimodal and show no anomalous tails or bimodality that would signal a localised area of newly solidified fine grains. Statistical data for the grain size distribution is presented in Table II. The continuous shift in grain-size distributions toward larger sizes indicates that microstructural evolution is governed by solid-state diffusion rather than by local melting and resolidification. However, it should be noted that grain size statistics represent bulk behaviour and may not capture extremely localised effects.

High-resolution EBSD IPF-Z maps focused on the most current-constricting areas are presented in Figure 10 for both perpendicular and parallel loading directions. In the EBSD map taken in the perpendicular direction for the sample sintered at 1350 °C (Figure 10(a)), the area enclosed/marked by the box contains a small particle of diameter approximately

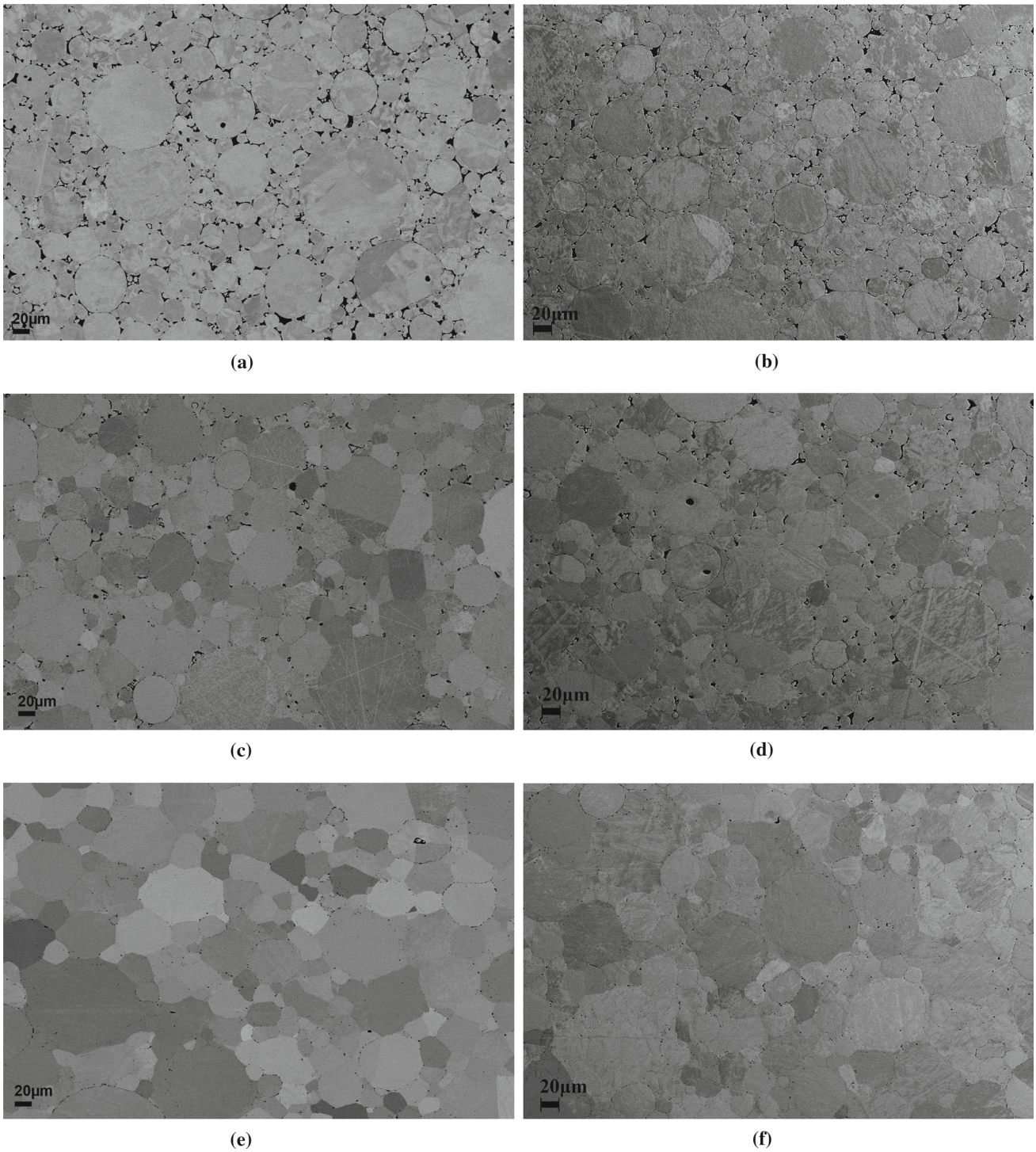

Fig. 6—SEM images of samples sintered at different temperatures: (*a*, *b*) 1350 °C, (*c*, *d*) 1450 °C, and (*e*, *f*) 1550 °C. Left column (a, c, e): cross-sections normal to the loading direction. Right column (b, d, f): cross-sections parallel to loading direction.

5 μm in between larger neighbours of around 70 μm (diameter ratio about 14:1). The same image also shows a second boxed region with a small particle surrounded by three big particles—a configuration/geometry commonly considered highly susceptible to contact resistance and local Joule heating. Similarly, in the EBSD map of cross-section parallel to the loading direction (Figure 10(b)), the marked area shows a small particle between large particles. In all the marked areas, all the particles have distinct crystallographic orientations and sharp grain-boundary outlines. No orientation inheritance (epitaxial growth) or localised fine equiaxed grains can be seen, which would indicate melting and resolidification. Figures 10(c) and (d) show the maps of the sample sintered at 1450 °C. Herein, small particles can be seen slightly indented into adjacent particles.

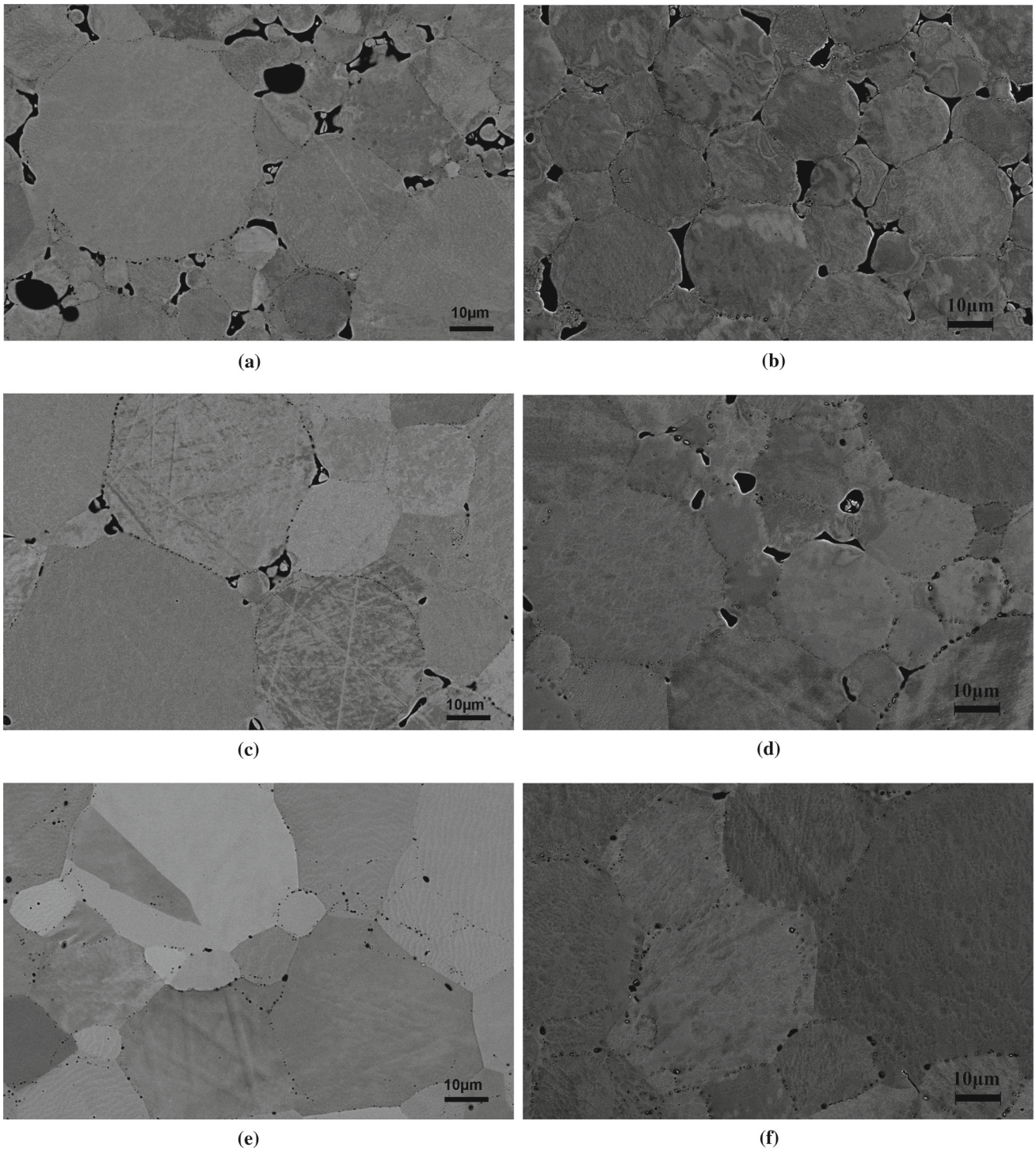

Fig. 7—High magnification SEM images of samples sintered at different temperatures: (*a*, *b*) 1350 °C, (*c*, *d*) 1450 °C, and (*e*, *f*) 1550 °C. Left column (a, c, e): cross-sections normal to the loading direction. Right column (b, d, f): cross-sections parallel to loading direction.

However, the maps from both cross-sections show independent crystal orientations (no epitaxy). Figures 10(e) and (f) present the maps of the sample sintered at 1550 °C. Despite being fully dense with faceted irregular grains, the small particles retain their own crystallographic orientations even where three particles meet, forming triple junctions. Overall, the high-resolution EBSD results are essentially the same in both perpendicular and parallel directions and do not reveal microstructural features that would be consistent with local melting or resolidification in the sintered NiAl samples under the investigated conditions.

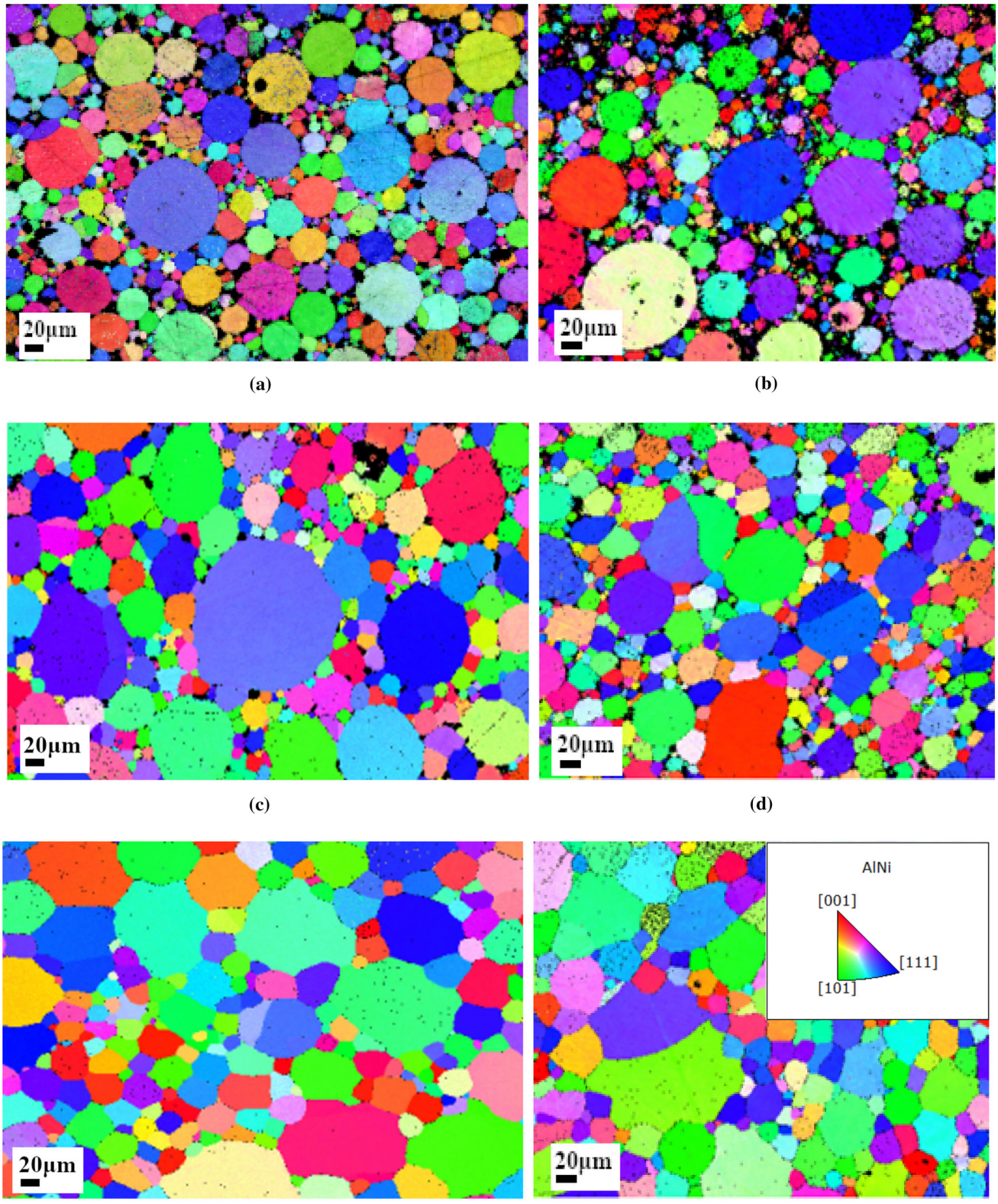

Fig. 8—EBSD (IPF-Z) maps of samples sintered at different temperatures: (*a*, *b*) 1350 °C, (*c*, *d*) 1450 °C, and (*e*, *f*) 1550 °C. Left column (a, c, e): cross-sections normal to the loading direction. Right column (b, d, f): cross-sections parallel to loading direction.

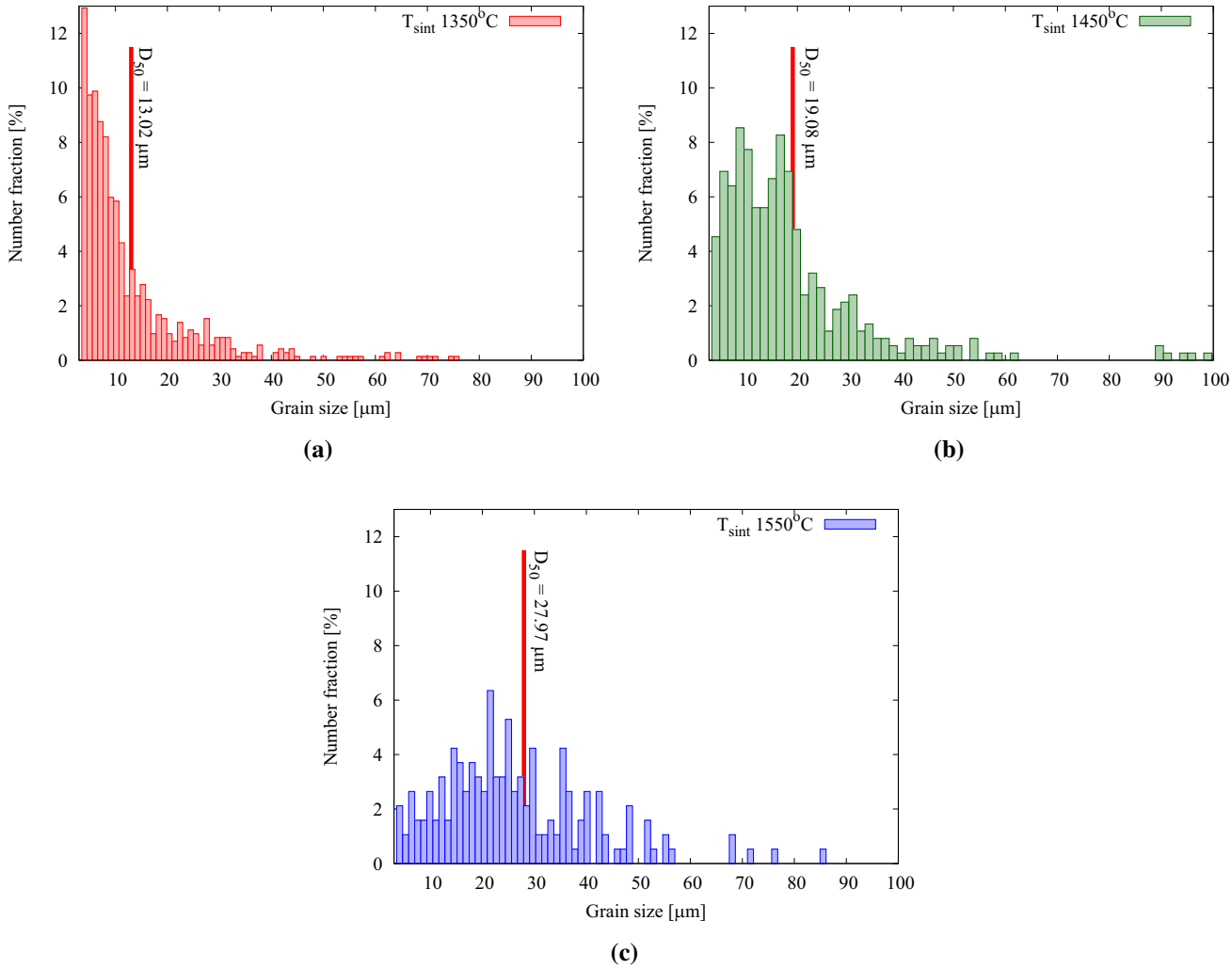

Fig. 9—Grain size distribution of samples sintered at: (*a*) 1350 °C, (*b*) 1450 °C, and (*c*) 1550 °C.

Table II. Statistical Analysis of Grain Size Distribution at Different Sintering Temperatures

Parameter	Description	1350 °C	1450 °C	1550 °C
D_{50}	volume average (μm)	13.02	19.08	27.97
σ	standard deviation (μm)	12.05	16.23	18.93
CV	coefficient of variation	0.93	0.85	0.68

IV. NUMERICAL STUDIES

Thermoelectric analyses, considering electric current flow, Joule heat generation, and heat conduction, were performed to assess temperature non-uniformity and the possibility of local overheating due to the concentration of electric current density at the necks or in small particles within heterogeneous particle configurations. Simulations were performed on geometries of equal-sized and three unequal-sized particles connected by the necks. The analysed problems were aimed to reproduce thermoelectric phenomena induced by an electric current flow through chains of particles in the consolidated powder. Equal-sized particles were analysed in two configurations, one representing a straight line chain and the other a zig-zag chain of particles.

The problem of equal-sized particles allows us to assess the temperature increase at the necks, while the case of unequal-sized particles, with a smaller particle between larger ones, enables us to estimate temperature non-uniformity in a heterogeneous microstructure.

In the numerical studies, we did not consider mechanical effects or electromechanical coupling, such as electroplasticity or pressure dependence of the electric contact resistance. We analysed the thermoelectric phenomena at fixed configurations corresponding to

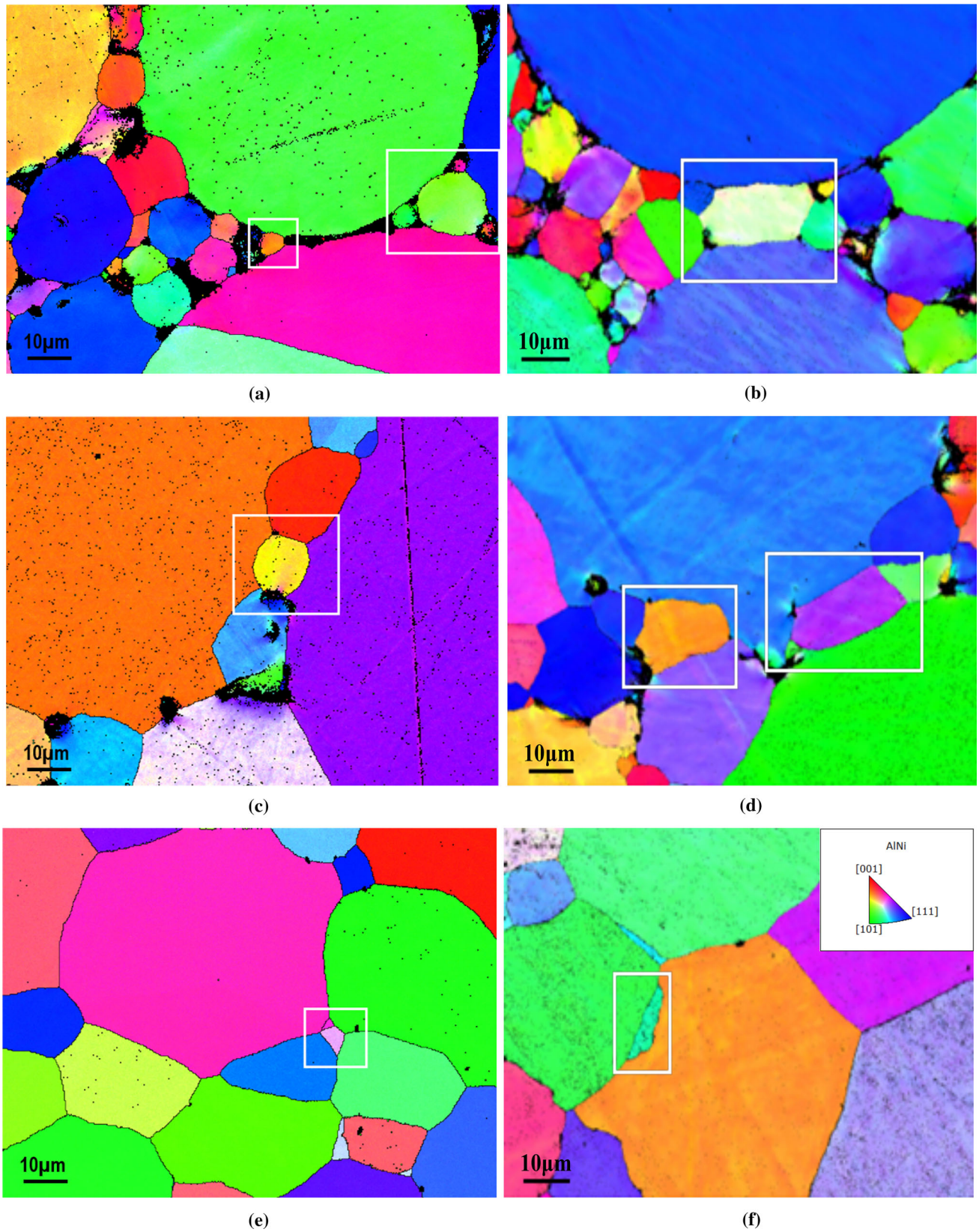

Fig. 10—High magnification EBSD (IPF-Z) maps of samples sintered at different temperatures: (*a*, *b*) 1350 °C, (*c*, *d*) 1450 °C, and (*e*, *f*) 1550 °C. Left column (a, c, e): cross-sections normal to the loading direction (step size 0.78 μm). Right column (b, d, f): cross-sections parallel to loading direction (step size 0.4 μm).

specific particle configurations during the sintering process. We investigated the thermoelectric problems occurring in short time intervals, which allowed us to assume the fixed configuration.

The thermoelectric analysis was performed using the finite-element software ABAQUS/CAE Standard 2024. The particles in a straight-line chain, both equal- and unequal-sized ones, were analysed using a 2D axisymmetric model. The problem of the particles in a zig-zag chain was solved using a general 3D model. The 2D geometry was discretised with four-node bilinear quadrilateral axisymmetric (DCAX4E) elements. The general 3D models were created using a 10-node quadratic tetrahedral (DC3D10E) elements.

The meshes were refined to ensure an accurate representation of the electric and thermal fields, particularly in the neck regions where current density and Joule heating are expected to be highest. A finer discretisation was used in the vicinity of the contacts and necks, while a coarser mesh was retained in regions farther from the interfaces to reduce computational cost. Four elements across the neck thickness and 160 elements along the neck radius were used. Based on our previous convergence studies in Reference 53, such a mesh is sufficient to give acceptable results. The appropriateness of the 3D model was assessed by comparing 3D and 2D axisymmetric solutions for a straight-line chain (see "Appendix C").

A. *Equal-Sized Particles in a Straight-Line Chain*

Thermoelectric phenomena related to the electric current flow through a chain of equal-sized particles in a straight line were analysed on the geometry of three aligned particles of radius r connected by the necks of radius a shown in Figure 11. The outermost particles were represented only by their hemispheres. Four different geometries consisting of three equal-sized particles, characterised by $r = 100$, 50, 10, and 2 μm, were analysed. The neck to radius a/r ratio of 0.05 was obtained by adjusting the particle overlaps h in accordance with Coble's sintering model[54]:

$$a = \sqrt{2hr}. \qquad [1]$$

An electric current in the axial direction was induced by the prescribed electric potential at the plane intersections passing through the centres of the top and bottom particles. The boundary-side surfaces were assumed to be electrically insulated. Joule heat generated by the constant current was absorbed and conducted through the particle volumes. The transient thermal problem was analysed assuming a certain uniform initial temperature and thermal insulation at the boundaries. The solution will provide the temperature increment. The temperature-independent properties were assumed for the analyses; therefore, for simplicity, we set the initial temperature to zero.

The following model parameters were used:

- density $\rho = 5910$ kg/m^3,
- specific heat capacity $c^{\text{th}} = 640$ J/(kg K),
- thermal conductivity $\kappa^{\text{th}} = 85$ W/(mK),
- electric conductivity $\kappa^{\text{el}} = 9.8\text{e}6$ S/m.

The electric and thermal conductivities of the grain boundaries are reduced due to disordered atomic arrangement, defects and impurities. The SEM and EBSD images presented above show that the layer with a distorted microstructure between the particles has a similar thickness for different necks and different particle sizes. We assume the same grain-boundary conductance $K_{\text{gb}}^{\text{el,th}}$ (given in W/(m^2 K)), for all the analysed cases, taking advantage of the calibration carried out in the previous works.[55,56] The conductance $K_{\text{gb}}^{\text{el,th}}$ of the grain-boundary layer with thickness δ_{gb} and conductivity $\kappa_{\text{gb}}^{\text{el,th}}$ is given as, cf. Reference 57:

$$K_{\text{gb}}^{\text{el,th}} = \frac{\kappa_{\text{gb}}^{\text{el,th}}}{\delta_{\text{gb}}}. \qquad [2]$$

The conductivities of the grain-boundary layer $\kappa_{\text{gb}}^{\text{el,th}}$ for given thickness δ_{gb} were determined in References 55 and 56 in terms of the reduction factors $\varepsilon^{\text{el,th}}$ and particle conductivities $\kappa^{\text{el,th}}$ as follows

$$\kappa_{\text{gb}}^{\text{el,th}} = \varepsilon^{\text{el,th}} \kappa^{\text{el,th}}, \qquad [3]$$

where

$$0 < \varepsilon^{\text{el,th}} < 1. \qquad [4]$$

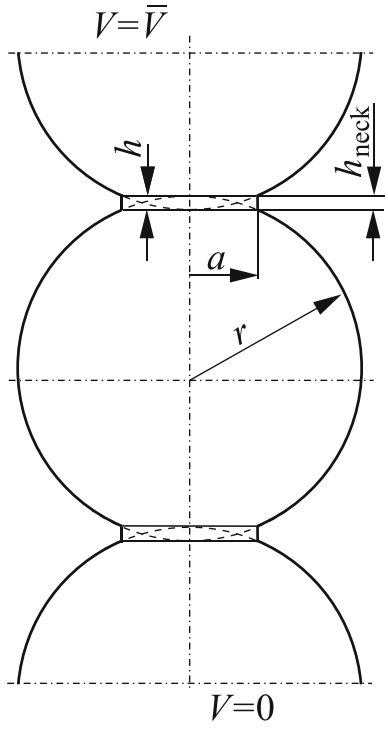

Fig. 11—Three equal particles—problem definition.

Table III. Reduced Thermal and Electrical Conductivities Assigned to the Elements in the Necks

r (μm)	h_{neck} (μm)	κ^{el}_{neck} (S/m)	κ^{th}_{neck} (W/m K)	$\bar{V}$ (V)
2	0.002503	1.704e4	0.180625	9.171e−5
10	0.012516	8.520e4	0.903125	2.440e−4
50	0.062580	4.260e5	4.515625	8.507e−4
100	0.125160	8.520e5	9.031250	1.605e−3

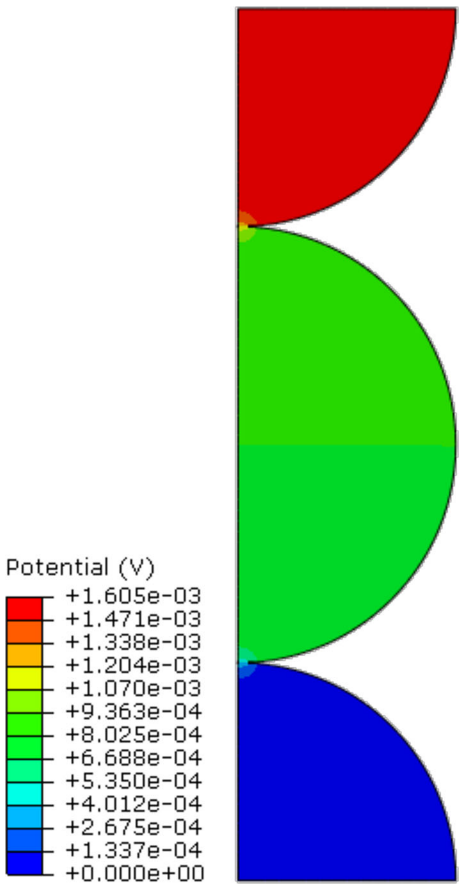

Fig. 12—Spatial distribution of the electric potential for $r = 100\,\mu$m.

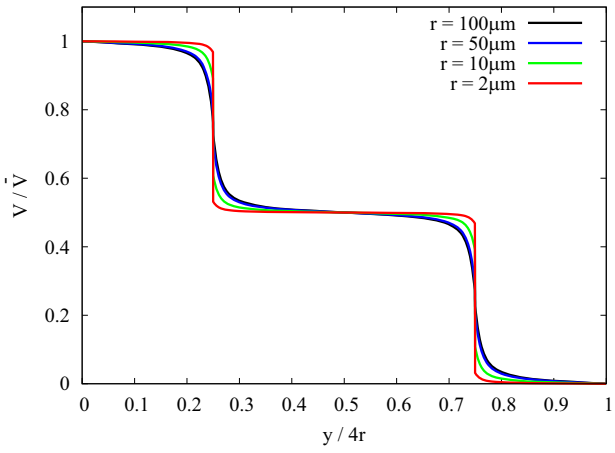

Fig. 13—Potential across the three particles.

The calibrated parameters for the electrical grain-boundary conductance are the following[56]: $\varepsilon^{el} = 0.16$ and $\delta_{gb} = 0.23\,\mu$m. The thermal grain-boundary conductance is evaluated using the following parameters[55]: $\varepsilon^{th} = 0.17$ and $\delta_{gb} = 0.2\,\mu$m.

The grain-boundary layer in the finite-element models has been considered using a diffused interface model,[57] taking the neck thickness h_{neck} as the thickness of the diffused interface. The conductivities in the neck are given as follows:

$$\kappa^{el,th}_{neck} = K^{el,th}_{gb} h_{neck}. \quad [5]$$

The neck height results from the geometrical construction. Its value for larger particles in our model is close to the grain boundary thickness calibrated in References 55 and 56. Geometrical construction of the necks for smaller particles, as well as the necks in the model of unequal-sized particles, gives lower values of the neck thickness. The conductivity in the diffused interface is adapted to keep the interface conductance and Joule heating unchanged. The values of the electric and thermal conductivities in the necks, calculated according to Eqs. [2] through [5], are given in Table III.

The prescribed values of electric potential at the top $\bar{V}$ for each geometry are given in Table III. $\bar{V}$ was evaluated to have the constant heating rate of approximately 185 °C/min in all the geometries. Note that this heating rate falls within the range typically used in real SPS processes.

The solution of the electric problem is presented in Figures 12, 13, 14, 15, and 16. Figure 12 shows the spatial distribution of the electric potential for $r = 100\,\mu$m. The electric problem analysed is a steady-state one: the distributions of electric potential and electric current, as well as Joule heating, are constant in time. Distributions of the electric potential along the axis of symmetry for the four analysed cases are compared in Figure 13. The voltage is normalised by the prescribed voltage $\bar{V}$ and the distance along the y-axis is normalised by four times the radius of the particle. This gives a better comparison of the voltage drop across geometries with different particle sizes. It can be observed that the voltage drops occur mostly at the necks. It is understandable, since the total voltage in a series circuit is distributed proportionally to the individual resistances, and the neck resistances are larger than those of the particle volumes. Furthermore, the smaller the particle size, the greater the voltage drop at the neck, as the neck resistance is comparatively higher.

A large change in voltage over a short distance results in a high potential gradient, leading to high electric current density (ECD) at the necks, especially at the neck boundary as shown in Figure 14. The concentration in this region is caused by two effects. The first one is the geometric constriction effect. Current flowing from one particle to the other must squeeze through the tiny contact area between touching spheres. The second effect arises from the interface separating materials with different resistivities, the particle and the neck. The normal components of the ECD on both sides of the

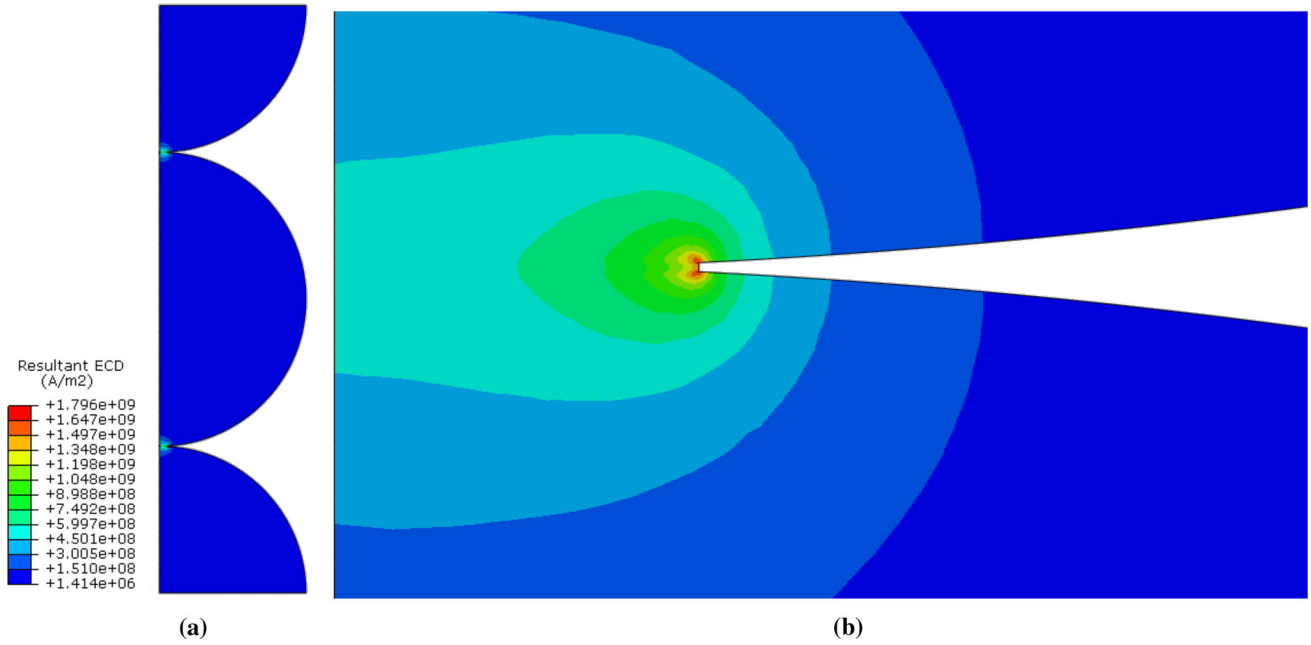

Fig. 14—Spatial distribution of the electric current density for $r = 100\,\mu$m: (*a*) in the whole geometry, and (*b*) in the neck area.

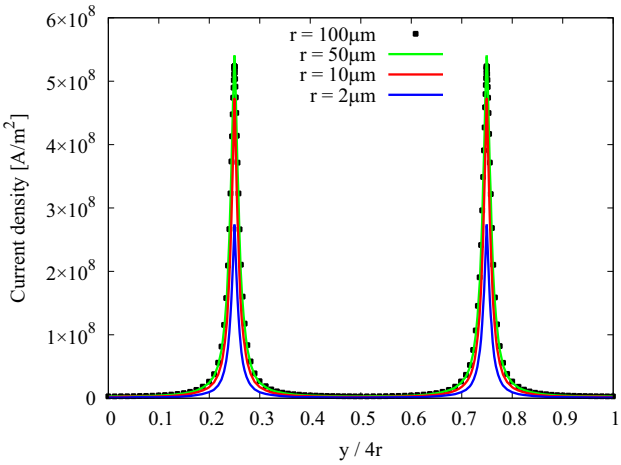

Fig. 15—Electric current density along the *y*-axis for different particle radii.

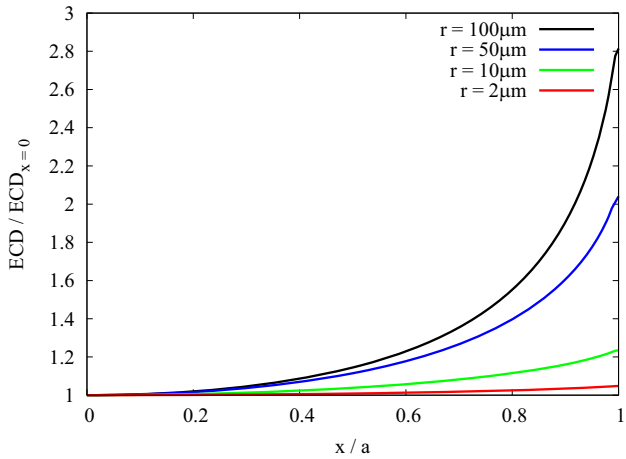

Fig. 16—Electric current density along the neck radius for different particle radii.

interface must be equal. However, the tangential components of the ECD are inversely proportional to the material's resistivity.[58] It can be seen in Figure 14 that a higher concentration is on the side of the particles, which have a lower resistivity than the neck. Figure 15 presents the ECD along the axis of symmetry for different particle sizes, highlighting the ECD peaks at the necks. The concentration of the ECD is highest at the neck boundary as shown in Figure 16, where ECD increases along the *x*-axis. Note that the ECD is normalised by the minimum ECD at $x = 0$, and distance along the *x*-axis normalised by neck radius *a*. It shows that the current density difference along the neck radius is higher when the particle size is larger.

Higher electric current density in the necks corresponds to greater heat generation and higher temperature increments in the necks, which can be observed in Figure 17. Joule heat generation leads to a continuous increase in temperature in the particles. Figure 18 gives the plots of temperature evolution in the particle centres for the four geometries. Due to thermal insulation of the boundaries and constant Joule heat generation, the temperature increase is linear except for a short initial period. The slopes of the lines represent a heating rate of approximately 180 to 190 °C/min.

As noted above, the temperature distribution is non-uniform. Variation of temperature increment along the axis of symmetry at time instant $t = 1$ ms for the four analysed cases is shown in Figure 19. The inter-particle neck regions exhibit higher temperatures than

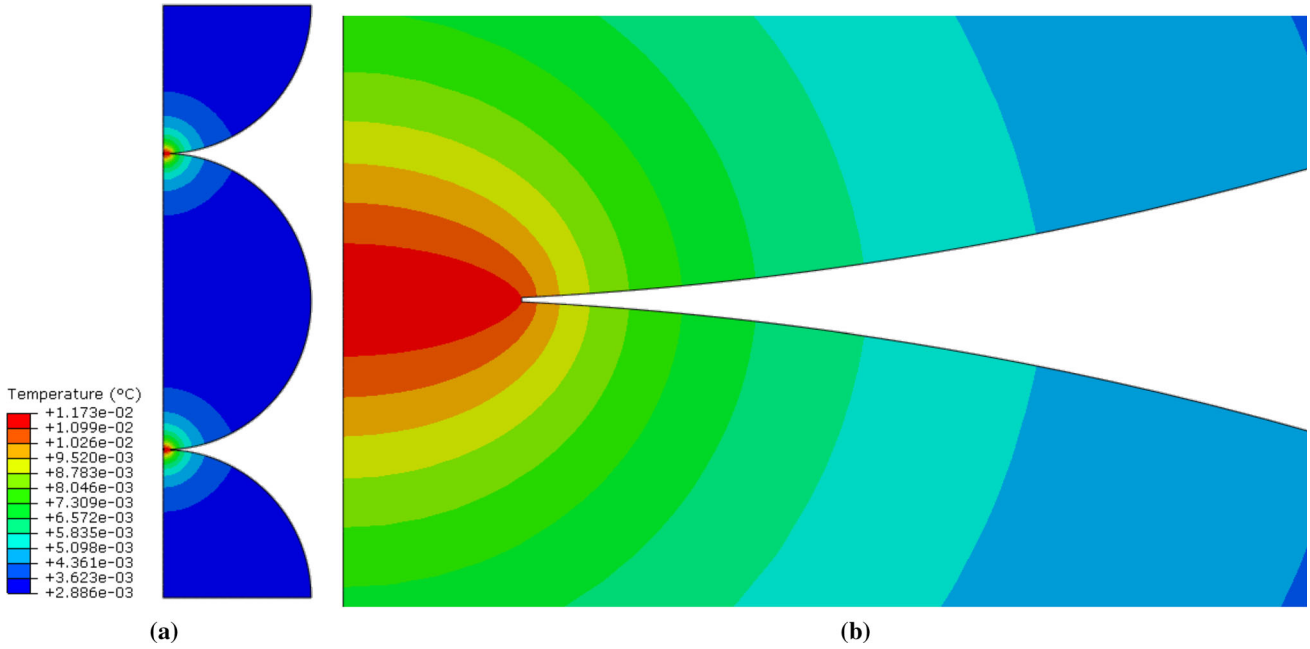

Fig. 17—Spatial temperature increment distribution for $r = 100\,\mu$m at t = 1 ms: (*a*) in the whole geometry, and (*b*) in the neck area.

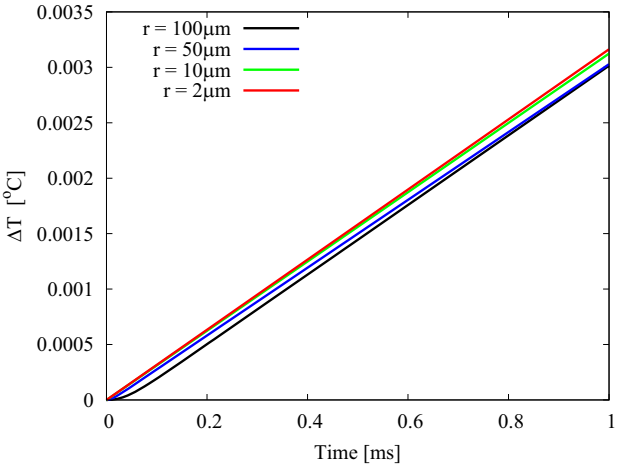

Fig. 18—Evolution of temperature increment in the particle centres.

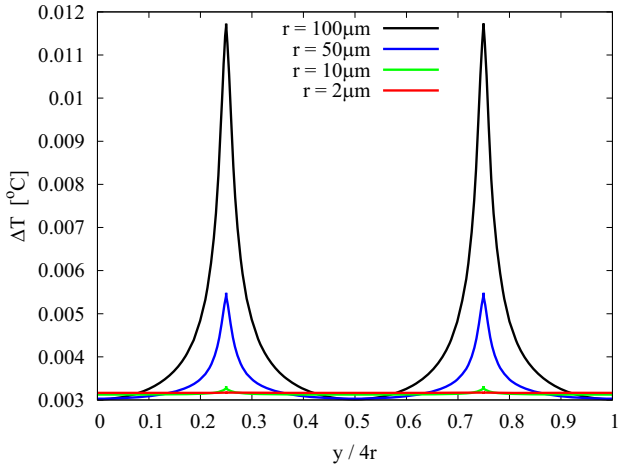

Fig. 19—Temperature increment along the y-axis at t = 1 ms.

the particle inner regions. Temporal evolution of the temperature difference between the centre and neck for different particle sizes is plotted in Figure 20. Starting from the uniform initial temperature, the temperature in the necks increases faster than the temperature at the particle centres due to enhanced Joule heat generation at the necks. However, at a certain stage, the difference does not increase anymore. This means that the developed temperature gradient ensures a uniform increase in temperature throughout the geometry. The steady-state temperature difference between the necks and particle centres increases with increasing particle size. Larger particles require more time for heat conduction within particles and therefore are more susceptible to overheating. However, the temperature difference is very low and would remain so if the analysis were extended to higher temperatures. Note that even with the largest particle size of 100 μm, the temperature difference is below 1 °C. This observation is in agreement with the other studies.[30,38,40] This analysis demonstrates that the heat generated in the necks is rapidly redistributed within the particles due to the high thermal conductivity of the considered material, and more precisely, to the high thermal diffusivity, which combines conductivity and heat capacity. This supports our experimental observation of the lack of local overheating traces in the investigated NiAl samples.

B. *Equal-Sized Particles in a Zig-Zag Chain*

Coupled thermoelectrical phenomena induced by the electric current flowing through a periodic zig-zag chain of equal-sized particles. The unit cell of the chain is given in Figure 21. The chain is parallel to the direction

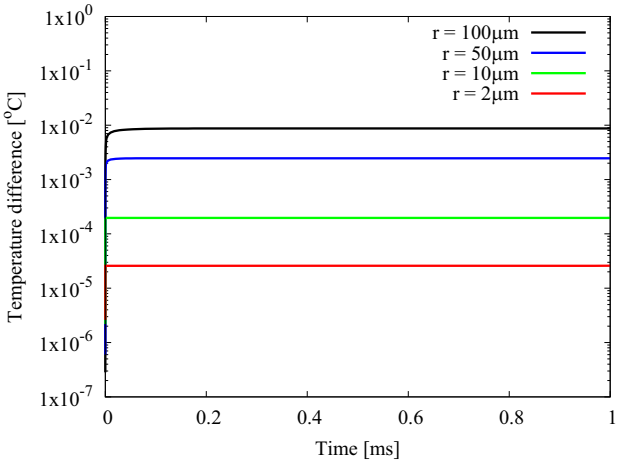

Fig. 20—Temporal evolution of temperature difference between the centre and neck.

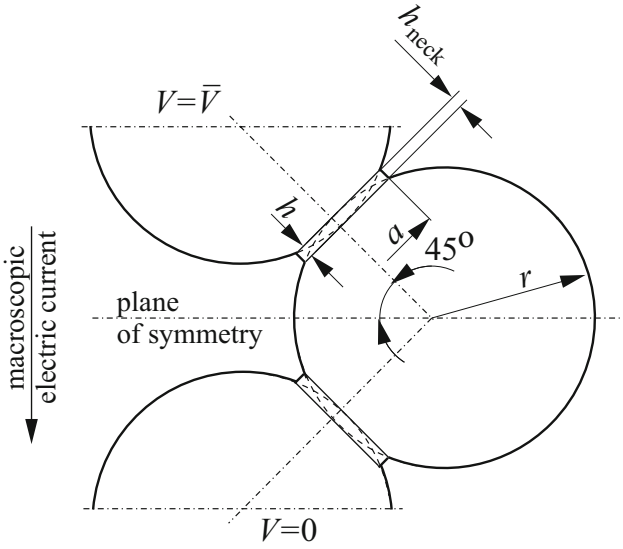

Fig. 21—Unit cell of a periodic zig-zag chain of bonded equal-sized particles.

of the macroscopic electric current. The particles of radius $r = 100\,\mu$m are bonded by the necks of radius a oriented at 45 deg to the macroscopic electric current. The ratio $a/r = 0.05$ is the same as that used in the model of straight line chain analysed in Section IV–A.

The same material properties as in the straight line chain have been used. The neck properties were taken the same as in the case of the particles of radius $r = 100\,\mu$m. This geometry requires a full 3D model. Taking advantage of the plane of symmetry, the finite element model was built for the half of the geometry shown in Figure 21. Accordingly, half of the voltage was prescribed. As before, the boundary-side surfaces were assumed to be electrically insulated, and thermal insulation at the boundaries was prescribed. The appropriateness of the 3D model was verified by comparison between the 3D and 2D axisymmetric solutions for particles in the straight-line chain, as presented in "Appendix C".

The electric and thermal fields in the particles in the zig-zag chain are depicted in Figures 22 and 23, respectively. Figure 22 shows that the electric potential is uniform in most of the particle volumes, and its gradient is localised in the neck area. Temperature increment localisation in the neck region is shown in Figure 23. Due to heat diffusion, the spatial extent of the temperature rise is wider than that of the electric potential gradient. The effect of the neck orientation is manifested in the spatial distribution of the temperature increment in Figure 23. However, the temperature increment profile along the line connecting the particle centres is very similar to the profile along the line connecting the centres of the particles in the straight line chain, as demonstrated in Figure 24. This is due to the fact that the voltage between particle centres is the same in both compared cases. In a real granular sample, the local electric field will depend on the orientation of particle pairs and necks relative to the applied macroscopic electric field, leading to differences in heat generation.

C. *Chain of Three Unequal-Sized Particles*

This example is aimed at investigating the effect of the particle size on Joule heating and temperature distribution. The electrical or thermal resistance of a sphere of radius r and conductivity κ between two equal-sized circular contacts with radius a at its poles is given analytically as follows, cf. References 59 and 60:

$$R = \frac{1}{\pi\kappa}\left[\frac{1}{a} + \frac{1}{2r}\left(\ln\frac{4r}{a} - 1\right)\right]. \qquad [6]$$

The second term in Eq. [6] introduces the dependence of the sphere resistance on its size; nevertheless, if $a \ll r$ the term $1/a$ predominates over the second term and the resistance of the sphere with flattened poles can be approximated as, cf. Reference 59:

$$R \approx \frac{1}{\pi\kappa a}. \qquad [7]$$

In view of Eq. [7], if we take two particles of different sizes but the same contact area, they will have nearly the same resistance. If the electric current flows through a chain of contacting particles of different sizes, the amount of heat generated by the current should be the same in the particles with the same contact area. However, the specific Joule heating (Joule heating per unit volume) will be higher in smaller particles, namely, it will be inversely proportional to the volume and to the cube of the radius.

Thermoelectric analysis has been performed for a system of three aligned, unequal-sized particles connected by necks, shown in Figure 25. The outer particles have radius of $r_i = 100\,\mu$m, and the central particle radius is $r_j = 6.25\,\mu$m. The central and outer particles are connected by the necks with radius $a = 0.5882\,\mu$m and height $h_{\text{neck}} = 0.02947\,\mu$m. The model is characterised by a significant difference in particle size $r_i/r_j =$

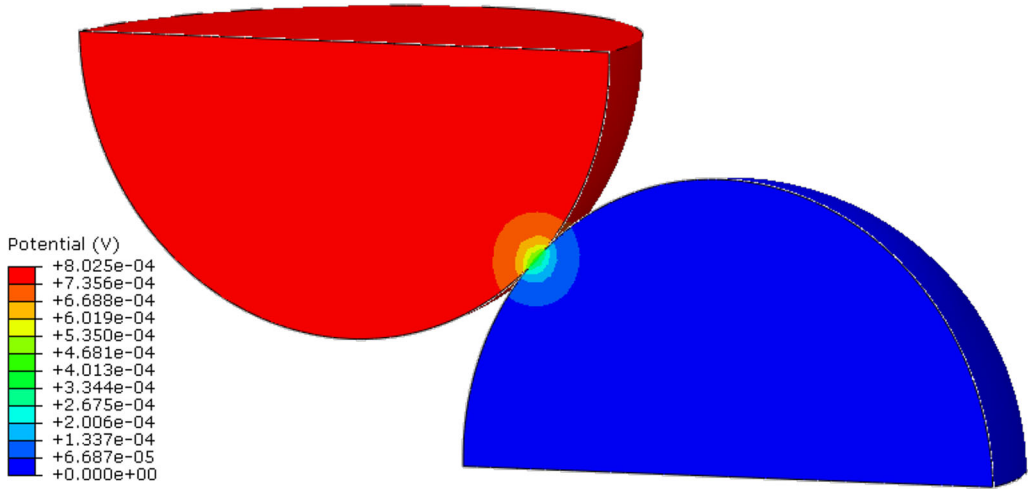

Fig. 22—Spatial distribution of the electric potential in the particles.

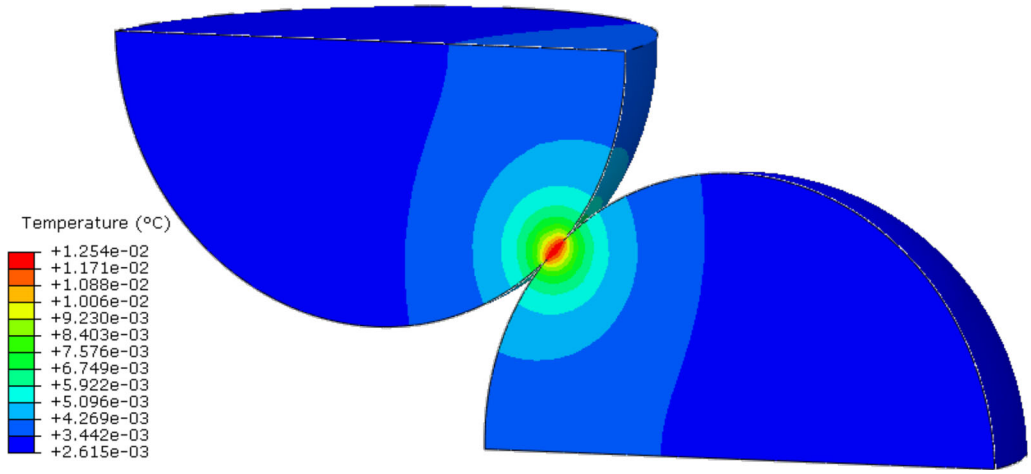

Fig. 23—Spatial distribution of the temperature increment in the particles.

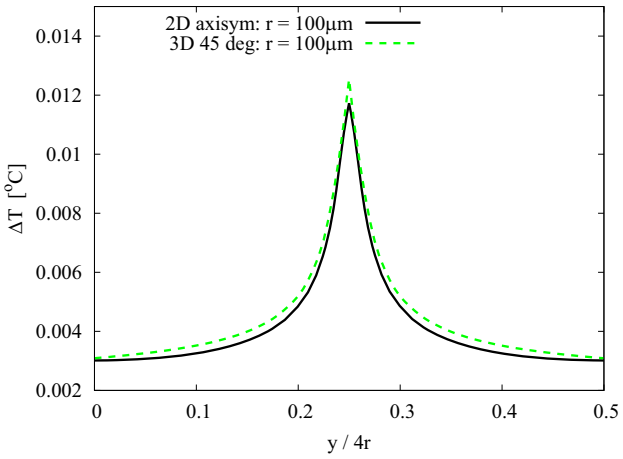

Fig. 24—Temperature increment along the line connecting particle centres at $t = 1$ ms—comparison between the 3D solution for the zig-zag chain and 2D axisymmetric solution for the straight line chain.

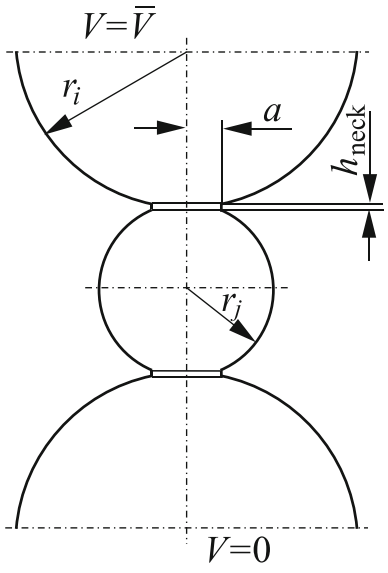

Fig. 25—Three unequal particles—problem definition.

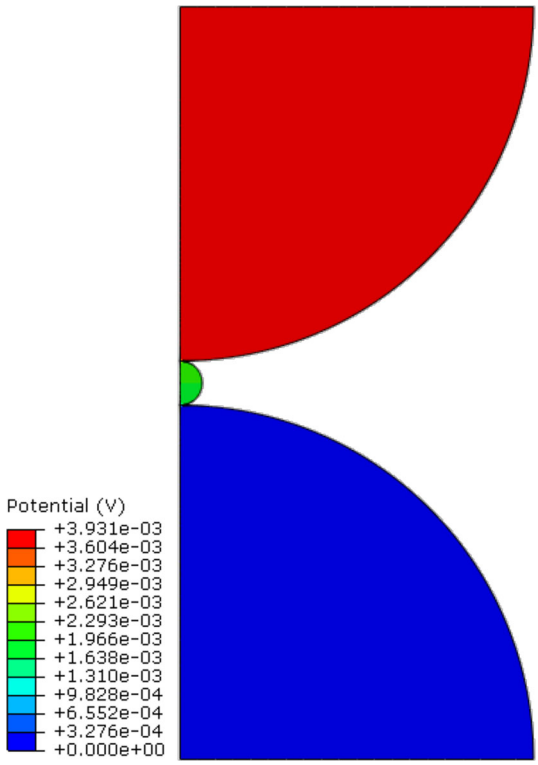

Fig. 26—Spatial distribution of the electric potential in three unequal-sized particles.

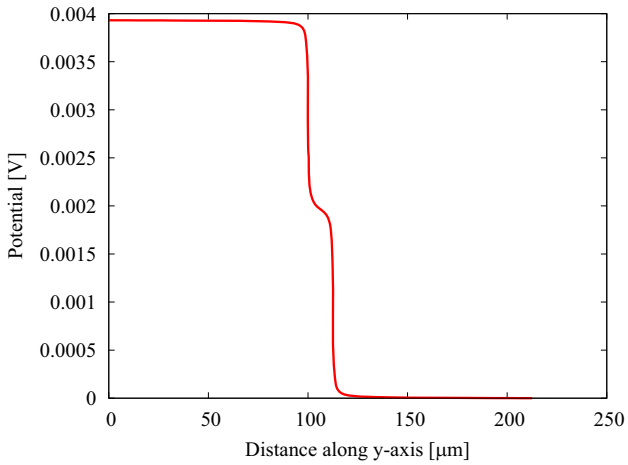

Fig. 27—Variation of the electric potential along the axis of symmetry.

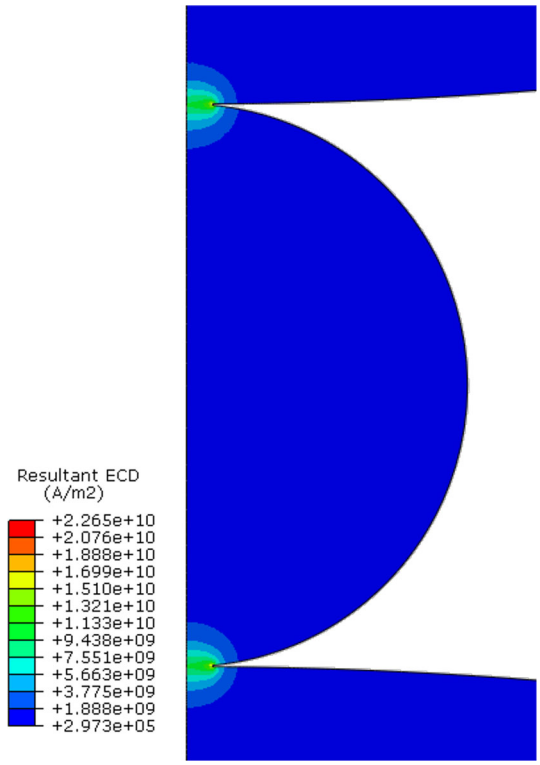

Fig. 28—Spatial distribution of the electric current density.

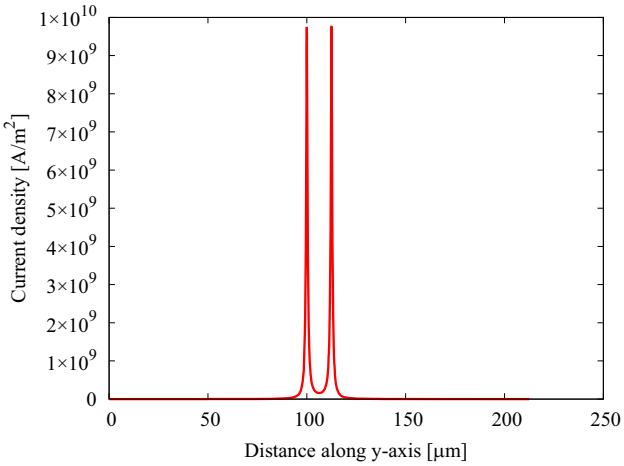

Fig. 29—Variation of the electric current density along the axis of symmetry.

16 and a very small neck size (the ratio $a/r_j = 0.09408$), which should create favourable conditions for overheating.

Thermal and electrical properties of the particles were the same as in the previous example. Reduced electrical and thermal conductivities assigned to the elements in the necks were obtained using Eq. [5] as $\kappa^{\text{el}}_{\text{neck}} = 4.9\text{e}5$ S/m and $\kappa^{\text{th}}_{\text{neck}} = 4.25$ W/(m K). Voltage of 3.9314×10^{-3} V was applied. The electric potential was prescribed at the top and bottom planes, and the side surfaces were electrically insulated. A uniform zero initial temperature was assumed. Thermal insulation was assumed for all the boundaries.

The solution to the electrical problem is presented in Figures 26, 27, and 28. Figure 26 illustrates the spatial distribution of the electric potential. The electric potential distributions along the axis of symmetry are given in Figure 13. The voltage drop occurs primarily at the neck regions since the necks exhibit higher resistance than the particle volumes. Large change of the electric potential over the small neck thickness produces a high potential gradient, leading to an elevated electric current density in the neck regions, as shown in Figure 28. Figure 29

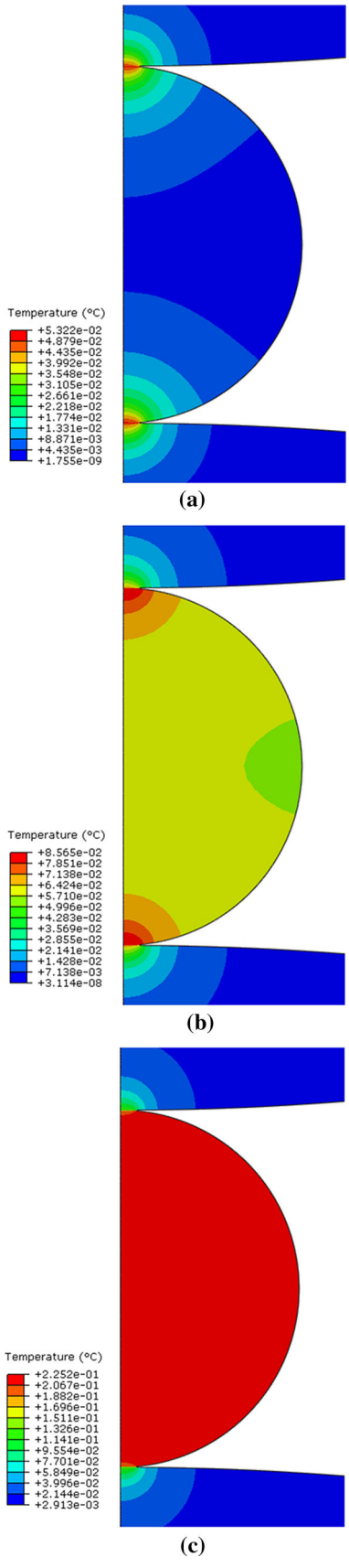

Fig. 30—Temporal evolution of temperature field in three particles: (*a*) t = 7e−7s, (*b*) t = 1e−6s, and (*c*) t = 1e−3s.

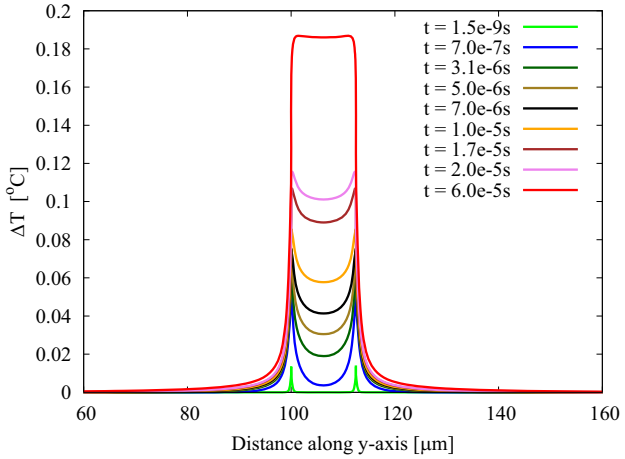

Fig. 31—Temporal evolution of temperature distribution along the axis of symmetry.

further demonstrates that the current density is particularly concentrated at the necks. The analysed electrical problem is steady-state; therefore, the distributions of electric potential, electric current density, and Joule heating remain constant over time.

The temperature field obtained in the solution of the thermal problem coupled with the electrical one evolves in time, which can be observed in Figures 30 and 31. Initially, the temperature in the necks grows faster than in the particles, due to the concentration of Joule heat generation in the necks. Joule heating causes a continuous rise in particle temperature as well, and the temperature in the central particle increases faster than in the outer particles. The central particle is smaller, so heat conducted from the necks heats it up more quickly. Joule heating in the smaller particle is more intense as discussed above. The neck, due to its high resistance, impedes heat flow between particles, which also favours an increase in temperature in the small particle. On the other hand, with the increase in temperature in the neck, the temperature gradient towards outer particles increases, so heat is conducted faster from the necks to the larger particles. This explains why at a certain time the temperature of the small particle achieves the level of temperature in the neck and even slightly exceeds it, and stabilises at a certain level cf. Figure 32. Figure 18 presents the temperature evolution at the particle centres for the three geometries. It can be observed that, after an initial period, the temperatures in the particles and the necks increase linearly. This indicates that the resulting temperature gradient promotes a uniform rise in temperature across the entire geometry. The heating rate in this stage is 194 °C/min. The difference in temperature between the central and outer particles remains unchanged, as it is shown in Figure 34, and it would remain so if the analysis were extended to higher temperatures This example demonstrates the possibility of overheating in very small particles placed between larger particles; however, the temperature difference is very small, and it is unlikely to cause local melting (Figure 33).

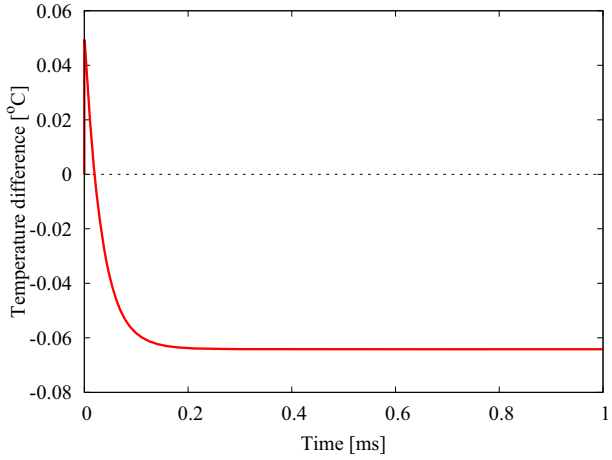

Fig. 32—Temperature difference between the neck and centre particle in the initial stages of simulation.

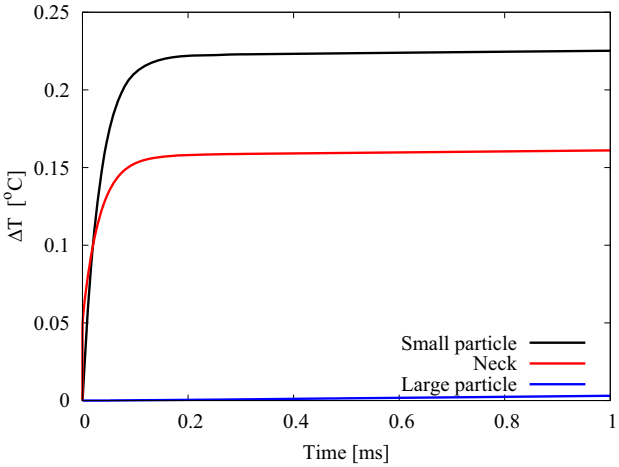

Fig. 33—Temperature evolution in unequal particles.

V. CONCLUSIONS

This work examined the potential for local overheating in NiAl during spark plasma sintering through a combined experimental and numerical approach. NiAl powder was sintered at 1350 °C, 1450 °C and 1550 °C, and additionally low-temperature and low-pressure conditions were examined to capture the early stages of densification. A broad size distribution of the starting powder, ranging from approximately 1 to 100 μm, enabled us to study the effect of heterogeneity on the local increase in temperature.

SEM and EBSD analysis, performed in both perpendicular and parallel loading directions, showed a continuous microstructural evolution with sintering temperature. At lower temperatures, the samples retained a more particle-like morphology with limited neck growth, whereas at higher temperatures, the contact regions became more faceted and the grains more coalesced, resulting in densification and grain growth. Across all conditions, however, no apparent

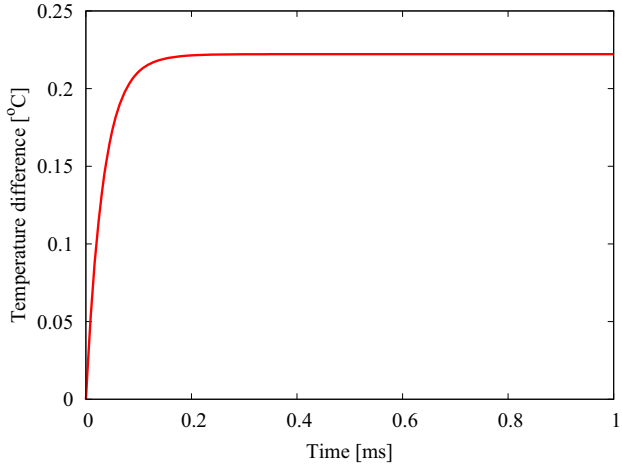

Fig. 34—Temperature difference between the central and outer particles.

microstructural evidence of local melting in NiAl samples sintered at temperatures up to 1550 °C was observed. Features typically associated with overheating—such as melt pools, epitaxial resolidification, or fine equiaxed grains—were absent, even in regions most susceptible to current concentration, including triple junctions, interparticle necks, and small particles located between larger particles.

The supplementary melted reference provided in "Appendix A" serves as a useful benchmark for melt-related morphology, while the supplementary XRD analysis presented in "Appendix B" is consistent with the overall microstructural observations. XRD analysis revealed pronounced crystallographic texture exclusively in the melted sample, whereas the sintered materials remained texture-free and exhibited narrow diffraction peaks.

Particle-scale thermo-electric simulations further support the experimental findings. The geometries of three equal-sized particles, arranged in a straight line and in a zig-zag chain, with additional grain-boundary resistance at the contacts, showed negligible temperature differences between the necks and particle centres, although the current density concentrated at the necks. It was observed that with increasing particle size, the temperature difference between the neck and particle centres increased. However, the temperature difference still remained below 1 °C even for the largest particle size of 100 μm. This indicates efficient heat dissipation within the particles, preventing the development of significant local overheating.

Numerical simulation on a heterogeneous configuration, involving a small particle confined between larger ones, showed susceptibility to localised temperature increase due to restricted heat conduction. It was observed that heat was generated in the necks and conducted to the particles; however, because of the small particle located between them, heat conduction to the larger particle was slower, eventually leading to an increase in the temperature of the small particle. Nevertheless, the temperature difference between the

small and large particles was still less than 0.25 °C and stayed constant in time. Examining this geometry provides new, experimentally relevant insights into how particle-size heterogeneity affects local Joule heating, transient temperature differences, and the effectiveness of heat conduction during heating.

Taken together, the experimental and numerical results demonstrate that, under the investigated conditions, spark plasma sintering of NiAl does not lead to significant or detectable local overheating and melting. This resolves an important question of local overheating in SPS processing of NiAl and provides a firm basis for simplifying SPS process models for similar materials.

ACKNOWLEDGMENTS

The authors acknowledge the National Science Centre, Poland funding within Research Project No. 2019/35/B/ST8/03158. The first author acknowledges the financial support provided by KMM-VIN Fellowship 2024 for the research work performed at Fraunhofer Institute for Ceramic Technologies and Systems (IKTS), Dresden. The authors thank Jan Räthel for hosting the first author to IKTS and for his support and guidance throughout the project. We also appreciate the help of Arkadiusz Gradys in performing X-ray diffraction.

FUNDING

The authors received financial support from the National Science Centre, Poland funding within Research Project No. 2019/35/B/ST8/03158. The first author received financial support from KMM-VIN Fellowship 2024 for the research work performed at Fraunhofer Institute for Ceramic Technologies and Systems (IKTS), Dresden.

DECLARATION OF AI-ASSISTED TECHNOLOGIES

During the preparation of this work the authors used ChatGPT (OpenAI) to improve language clarity and readability. After using this tool, the authors reviewed and edited the content as needed and take full responsibility for the content of the published article.

CONFLICT OF INTEREST

The authors declare that they have no conflicts of interest.

APPENDIX A: ANALYSIS OF THE PARTIALLY MELTED SAMPLE

Figure 35 shows the sample melted at 1620 °C. The sample can be used as a reference to identify microstructural features of melting in NiAl. The melted sample exhibits characteristic signatures of melting and

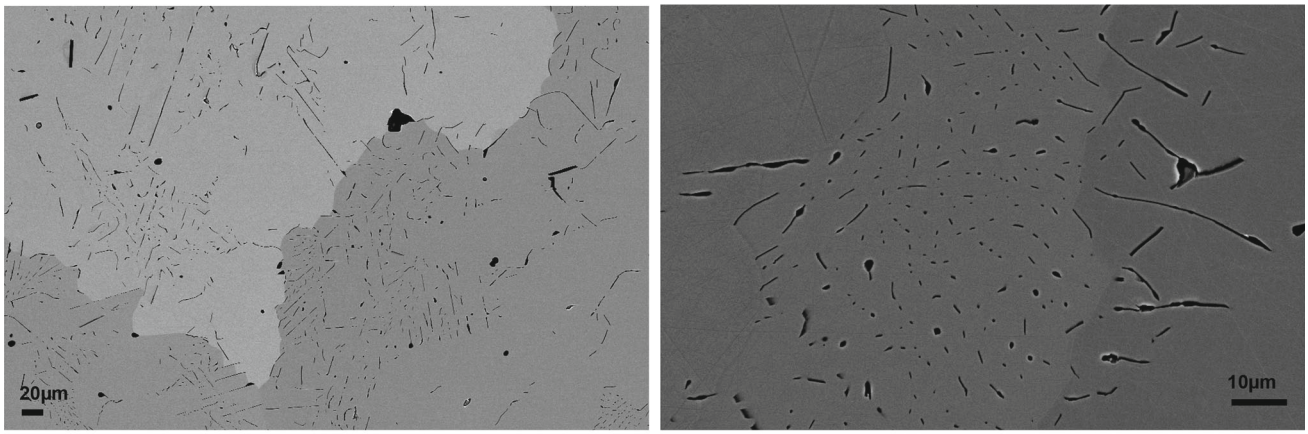

(a) (b)

Fig. 35—SEM images of sample sintered at 1620 °C (melted) (*a*) low magnification, and (*b*) high magnification.

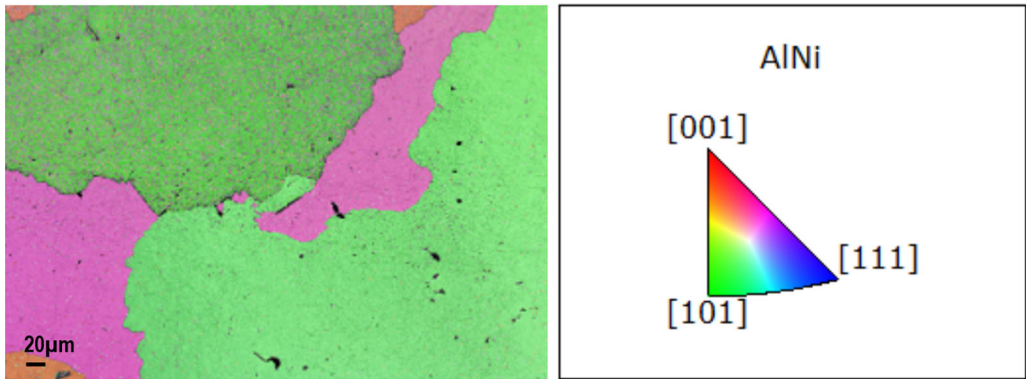

Fig. 36—EBSD map of sample sintered at 1620 °C (melted).

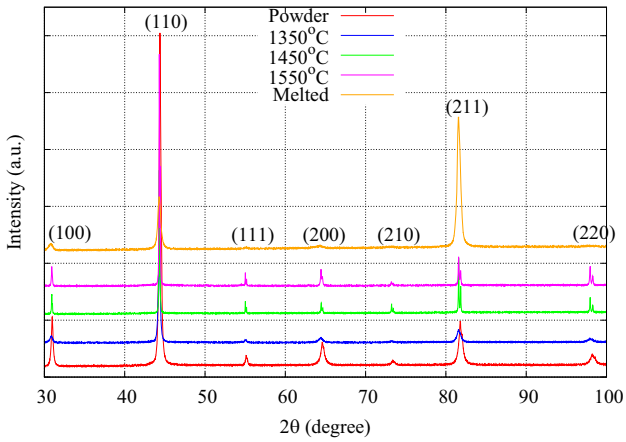

Fig. 37—XRD patterns of the starting powder, sintered compacts and melted reference sample.

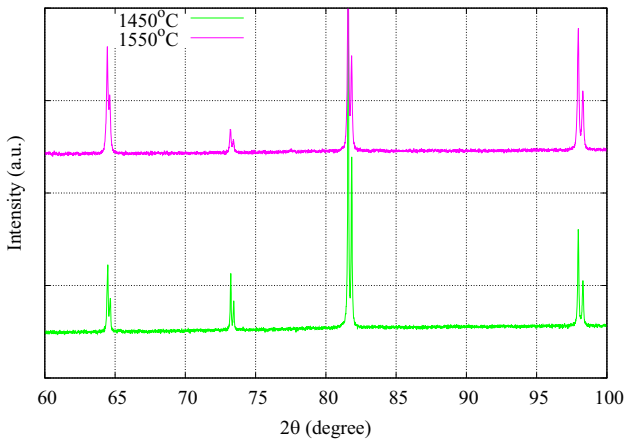

Fig. 38—Zoomed in XRD patterns showing $K\alpha_1/K\alpha_2$ peak splitting in samples sintered at 1450 °C and 1550 °C.

resolidification. The original spherical particle morphology (shown in Figure 1) has been largely removed, and distinct grain boundaries are not apparent. Small microcracks can also be seen in the resolidified sample, which could be due to solidification shrinkage and stress concentration during cooling. These observations are evidence of melting and are therefore referred to as flow-like features rather than solid-state sintering morphologies. This provides a visual contrast to the sintered samples shown in Figures 4, 5, 6, and 7.

Figure 36 presents EBSD map acquired for the reference sample melted at 1620 °C. The EBSD map of the melted reference (Figure 36) is dominated by a limited number of orientations, indicating the development of strong crystallographic texture during resolidification. The absence of the original particle morphology and the presence of large grains are consistent with solidification-driven microstructural evolution, providing a useful benchmark for identifying melting-related features.

APPENDIX B: X-RAY DIFFRACTION ANALYSIS

X-ray diffraction (XRD) results were obtained on Rigaku SmartLab 3 kW universal X-ray diffractometer with a vertical $\theta - \theta$ goniometer and a copper anode tube ($\lambda = 0.15418$ nm) as the radiation source. Phase analysis was performed using PDXL2 software (Integrated X-ray Powder Diffraction, version 2.8.3.0, Rigaku), which works with PDF-5+ 2026 crystallographic database (ICDD, International Centre for Diffraction Data).

XRD, being a bulk averaging technique, provides information on phases present in the melted and sintered samples. Phase changes visible in XRD patterns can also be the identifier of melting due to overheating in SPS-sintered materials. Partial melting followed by resolidification can change diffraction signals, such as peak broadening, detectable shifts in peak or emergence of second phases if significant compositional change or segregation occurs. Conversely, the absence of phase changes or abnormal peak broadening is evidence against local melting. Although XRD can not be used as a strong tool since the minimum detectable phase limit of 3 pct applies. However, for single-phase intermetallics, such as NiAl, local and transient melting should be easier to detect than in complex systems.

Figure 37 presents the XRD patterns for the starting powder, melted reference and the samples sintered at 1350 °C, 1450 °C and 1550 °C in the range of $2\theta = 30$ to 100 deg. Only reflections identified as NiAl B2 cubic structure can be seen in all the patterns. No additional

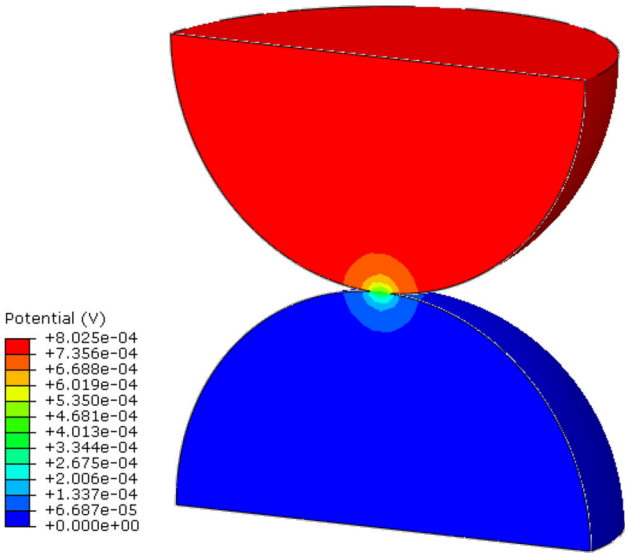

Fig. 39—Spatial distribution of the electric potential in the 3D solution for $r = 100\,\mu$m.

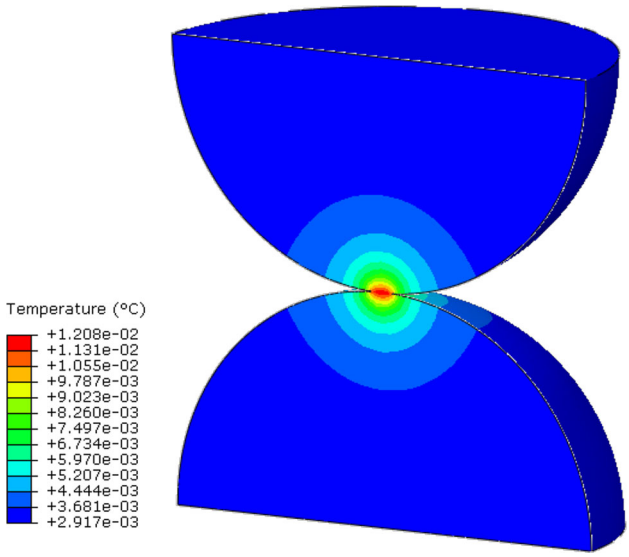

Fig. 40—Spatial distribution of the temperature increment in the 3D solution for $r = 100\,\mu$m.

phases were detected. However, it can be seen that the melted sample shows an imbalance in peak intensity. The (211) peak is unusually strong, while peaks other than for the (110) plane are barely visible. This suggests preferential orientation developed during resolidification. EBSD map of the same sample also shows two dominant crystal orientations. On the other hand, samples sintered at 1450 °C and 1550 °C show $K\alpha_1$ and $K\alpha_2$ peak splitting, which is visible in the zoomed plot in Figure 38. Narrower peaks and doublets indicate lower microstrain and a higher degree of structural order. This shows solid-state grain growth and recovery during sintering rather than a large number of resolidified fine grains (equiaxed), which would result in peak broadening. A small shift in peaks relative to the powder may indicate a slight change in the lattice parameter. Nevertheless, overall XRD results do not indicate melting followed by segregation or secondary phase formation. If local melting had produced appreciable amounts of new phases, we would expect to see extra peaks; none are observed.

APPENDIX C: VERIFICATION OF THE 3D MODEL

The 3D model was verified against the 2D axisymmetric model employed for equal-sized particles in the straight line chain. Figure 39 shows the spatial distribution of the electric potential in the 3D solution for $r = 100\,\mu$m. The solution can be compared with the 2D axisymmetric solution shown in Figure 12. It should be noted that the voltage prescribed in the 3D model is half that prescribed in the 2D axisymmetric model, since only half of the model is considered in the 3D analysis. Figure 40 presents the spatial distribution of the temperature increment. The temperature increment from the 3D model is compared with the 2D axisymmetric solution in Figure 41. A very good agreement

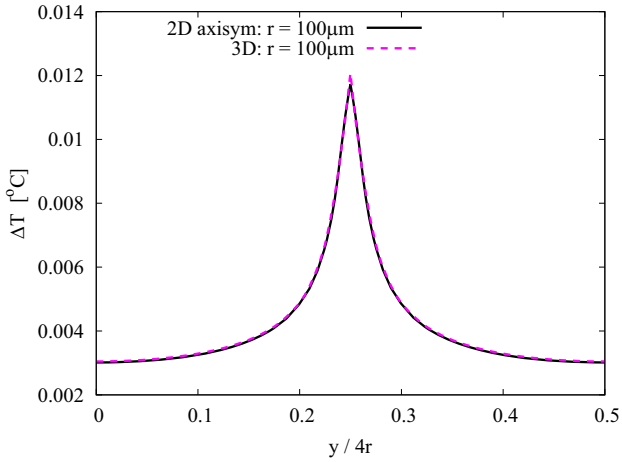

Fig. 41—Temperature increment along the y-axis at $t = 1$ ms—comparison between the 3D and 2D axisymmetric solutions.

between the two solutions confirms the appropriateness of the 3D model investigated here as well as of the model used in Section IV–B, which has a similar resolution.

REFERENCES

1. J.-P. Monchoux, A. Couret, L. Durand, T. Voisin, Z. Trzaska, and M. Thomas: *Metals*, 2021, vol. 11, pp. 1–20. https://doi.org/10.3390/met11020322.
2. K. Kaszyca, M. Chmielewski, B. Bucholc, P. Błyskun, F. Nisar, J. Rojek, and R. Zybała: *Materials*, 2024. https://doi.org/10.3390/ma17061422.
3. S. Nosewicz, P. Jenczyk, B. Romelczyk-Baishya, P. Bazarnik, D. Jarzabek, K. Majchrowicz, Z. Pakieła, K. Kowiorski, and M. Chmielewski: *Mater. Sci. Eng. A*, 2024. https://doi.org/10.1016/j.msea.2023.146001.
4. J. Wachowicz, J. Gos, and J. Wilkowski: *Structure and Cutting Properties of WC–CO Composites Obtained by the SPS-Spark Plasma Sintering Method*, Technical Report, Warsaw University of

Life Sciences, Forestry and Wood Technology (WULS-SGGW), 2021.
5. O. Guillon, J. Gonzalez-Julian, B. Dargatz, T. Kessel, G. Schierning, J. Räthel, and M. Herrmann: *Adv. Eng. Mater.*, 2014, vol. 16, pp. 830–49.
6. U. Anselmi-Tamburini: in *Encyclopedia of Materials: Technical Ceramics and Glasses*. M. Pomeroy, ed., Elsevier, Oxford, 2021, pp. 294–310. https://doi.org/10.1016/B978-0-12-803581-8.11730-8.
7. A.S. Semenov, J. Trapp, M. Nöthe, B. Kieback, and T. Wallmersperger: *Adv. Eng. Mater.*, 2023. https://doi.org/10.1002/adem.202300764.
8. R. Orrù, R. Licheri, A.M. Locci, A. Cincotti, and G. Cao: *Mater. Sci. Eng. R*, 2009, vol. 63, pp. 127–287. https://doi.org/10.1016/j.mser.2008.09.003.
9. S. Deng, H. Zhao, R. Li, T. Yuan, L. Li, and P. Cao: *Powder Technol.*, 2019, vol. 356, pp. 769–77. https://doi.org/10.1016/j.powtec.2019.08.108.
10. F. Nisar, J. Rojek, S. Nosewicz, K. Kaszyca, and M. Chmielewski: *Powder Technol.*, 2025, vol. 458, p. 120957. https://doi.org/10.1016/j.powtec.2025.120957.
11. X. Song, X. Liu, and J. Zhang: *J. Am. Ceram. Soc.*, 2006, vol. 89, pp. 494–500. https://doi.org/10.1111/j.1551-2916.2005.00777.x.
12. H. Ammari, S.L. Gallet, P.H. Cornuault, F. Herbst, N. Geoffroy, M. Chemingui, and V. Optasanu: *Materials*, 2025. https://doi.org/10.3390/ma18245652.
13. T.T. Saravanan, M. Kamaraj, S.C. Sharma, S. Kumaran, V.S.K. Chakravadhanula, K.V. Ravikanth, K.V. Kumar, and H. Sreemoolanadhan: *Mater. Lett.*, 2020. https://doi.org/10.1016/j.matlet.2020.128150.
14. Z.-Y. Hu, Z.-H. Zhang, X.-W. Cheng, F.-C. Wang, Y.-F. Zhang, and S.-L. Li: *Mater. Des.*, 2020, vol. 191, p. 108662.
15. K. Bochenek and M. Basista: *Prog. Aerosp. Sci.*, 2015, vol. 79, pp. 136–46. https://doi.org/10.1016/j.paerosci.2015.09.003.
16. Z. Wen, Y. Zhao, H. Hou, J. Tian, and P. Han: *Superlattices Microstruct.*, 2017, vol. 103, pp. 9–18. https://doi.org/10.1016/j.spmi.2017.01.010.
17. Y. Yu, X. Cai, Z. Cao, X. Jiao, W. Xie, Y. Yu, and P. Feng: *Mater. Charact.*, 2022. https://doi.org/10.1016/j.matchar.2022.112062.
18. T.S. Ogneva, I.A. Bataev, V.I. Mali, A.G. Anisimov, D.V. Lazurenko, A.I. Popelyukh, Y.Y. Emurlaeva, A.A. Bataev, S. Tanaka, and K.D. Yegoshin: *Mater. Charact.*, 2021. https://doi.org/10.1016/j.matchar.2021.111415.
19. R. Darolia: *JOM*, 1994, vol. 43, pp. 44–49.
20. M. Shekari, M. Adeli, A. Khobzi, M. Kobashi, and N. Kanetake: *Adv. Powder Technol.*, 2017, vol. 28, pp. 2974–79. https://doi.org/10.1016/j.apt.2017.09.004.
21. M. Abedi, K. Kuskov, D. Moskovskikh, E.V. Zakharova, D. Belov, and A. Mukasyan: *Intermetallics*, 2023. https://doi.org/10.1016/j.intermet.2022.107750.
22. W. Chen, U. Anselmi-Tamburini, J.E. Garay, J.R. Groza, and Z.A. Munir: *Mater. Sci. Eng. A*, 2005, vol. 394, pp. 132–38. https://doi.org/10.1016/j.msea.2004.11.020.
23. M. Tokita: *Mater. Sci. Forum*, 1999. https://doi.org/10.4028/www.scientific.net/msf.308-311.83.
24. M. Tokita: *Ceramics*, 2021, vol. 4, pp. 160–98. https://doi.org/10.3390/ceramics4020014.
25. T. Saunders, S. Grasso, and M.J. Reece: *J. Eur. Ceram. Soc.*, 2014, vol. 35, pp. 871–77. https://doi.org/10.1016/j.jeurceramsoc.2014.09.022.
26. R. Marder, C. Estournès, G. Chevallier, and R. Chaim: *Scripta Mater.*, 2014, vol. 82, pp. 57–60. https://doi.org/10.1016/j.scriptamat.2014.03.023.
27. R. Marder, C. Estournès, G. Chevallier, and R. Chaim: *J. Eur. Ceram. Soc.*, 2015, vol. 35, pp. 211–18. https://doi.org/10.1016/j.jeurceramsoc.2014.08.001.
28. V.A. Kudryashov, S.M. Godin, S.G. Vadchenko, and A.S. Rogachev: *Instrum. Exp. Tech.*, 2020, vol. 63, pp. 77–80. https://doi.org/10.1134/S0020441220010157.
29. A.S. Rogachev, S.G. Vadchenko, V.A. Kudryashov, A.S. Shchukin, and M.I. Alymov: *Dokl. Phys. Chem.*, 2019, vol. 488, pp. 151–53. https://doi.org/10.1134/S001250161910004X.
30. J. Trapp and B. Kieback: *J. Am. Ceram. Soc.*, 2015, vol. 98(11), pp. 3547–52. https://doi.org/10.1111/jace.13757.
31. O. Yanagisawa, H. Kuramoto, K. Matsugi, and M. Komatsu: *Mater. Sci. Eng. A*, 2003, vol. 350(1–2), pp. 184–89.
32. N. Chawake, L.D. Pinto, A.K. Srivastav, K. Akkiraju, B.S. Murty, and R.S. Kottada: *Scripta Mater.*, 2014, vol. 93, pp. 52–55. https://doi.org/10.1016/j.scriptamat.2014.09.003.
33. S. Ghosh, A.H. Chokshi, P. Lee, and R. Raj: *J. Am. Ceram. Soc.*, 2009, vol. 92, pp. 1856–59. https://doi.org/10.1111/j.1551-2916.2009.03102.x.
34. M.S. Bernardo, T. Jardiel, A.C. Caballero, M. Bram, J. Gonzalez-Julian, and M. Peiteado: *J. Eur. Ceram. Soc.*, 2019, vol. 39, pp. 2042–49. https://doi.org/10.1016/j.jeurceramsoc.2019.01.045.
35. A. Zuniga, L. Ajdelsztajn, and E.J. Lavernia: *Metall. Mater. Trans. A*, 2006, vol. 37A, pp. 1343–52. https://doi.org/10.1007/s11661-022-06821-z.
36. T. Tomše, B. Podmiljšak, L. Scherf, R. Kessler, S. Kobe, A. Kocjan, S. Šturm, and K. Žužek: *J. Mater. Process. Technol.*, 2024. https://doi.org/10.1016/j.jmatprotec.2024.118405.
37. Y. Xia, J.L. Zhao, and M. Qian: *JOM*, 2019, vol. 71, pp. 2556–63. https://doi.org/10.1007/s11837-019-03590-w.
38. C. Collard, Z. Trzaska, L. Durand, J.-M. Chaix, and J.-P. Monchoux: *Powder Technol.*, 2017, vol. 321, pp. 458–70.
39. Z. Trzaska, C. Collard, L. Durand, A. Couret, J.M. Chaix, G. Fantozzi, and J.P. Monchoux: *J. Am. Ceram. Soc.*, 2018. https://doi.org/10.1111/jace.15999.
40. J. Trapp, A. Semenov, O. Eberhardt, M. Nöthe, T. Wallmersperger, and B. Kieback: *Powder Metall.*, 2020, vol. 63, pp. 312–28. https://doi.org/10.1080/00325899.2020.1829349.
41. Z. Trzaska and J.-P. Monchoux: *J. Alloys Compd.*, 2015, vol. 635, pp. 142–49. https://doi.org/10.1016/j.jallcom.2015.02.122.
42. Y. Imai and M. Kumazawa: *Sintered Intermetallic Compound NiAl as High Temperature Material. I. Technical Report, 938th Report of Research Institute for Iron, Steel and Other Metals*, 1959. https://tohoku.repo.nii.ac.jp/record/45440/files/KJ00004196798.pdf.
43. E. Kozlov, N. Popova, E. Nikonenko, M. Fedorischeva, N. Sizonenko, and N. Koneva: *AIP Conf. Proc.*, 2016, vol. 1783(1), p. 020111. https://doi.org/10.1063/1.4966404.
44. ASTM International, *Standard Test Methods for Density of Compacted or Sintered Powder Metallurgy (PM) Products Using Archimedes' Principle. Standard ASTM B962-13*, ASTM International, 2013. https://doi.org/10.1520/B0962-13.
45. D.V. Dudina, A.A. Shtertser, T.M. Vidyuk, and B.B. Bokhonov: *Int. J. Refract. Met. Hard Mater.*, 2024. https://doi.org/10.1016/j.ijrmhm.2024.106732.
46. T.M. Vidyuk, D.V. Dudina, M.A. Korchagin, A.I. Gavrilov, T.S. Skripkina, A.V. Ukhina, A.G. Anisimov, and B.B. Bokhonov: *Vacuum*, 2020. https://doi.org/10.1016/j.vacuum.2020.109566.
47. D.V. Dudina and N.Y. Cherkasova: *Mater. Lett.*, 2024. https://doi.org/10.1016/j.matlet.2024.136411.
48. I. Singh and V.V. Dabhade: *Int. J. Refract. Met. Hard Mater.*, 2024. https://doi.org/10.1016/j.ijrmhm.2024.106849.
49. T. Ishimoto, K. Hagihara, K. Hisamoto, and T. Nakano: *Addit. Manuf.*, 2021. https://doi.org/10.1016/j.addma.2021.102004.
50. X. Boulnat, M. Perez, D. Fabregue, T. Douillard, M.H. Mathon, and Y.D. Carlan: *Metall. Mater. Trans. A*, 2014, vol. 45A, pp. 1485–97. https://doi.org/10.1007/s11661-013-2107-y.
51. Q. Yang, T. Wojcik, and E. Kozeschnik: *Materials*, 2024, vol. 17, p. 4385. https://doi.org/10.3390/ma17174385.
52. S.D. Mesarovic and N.A. Fleck: *Int. J. Solids Struct.*, 2000, vol. 37, pp. 7071–91.
53. J. Rojek, R. Kasztelan, and R. Tharmaraj: *Powder Technol.*, 2022, vol. 405, p. 117521. https://doi.org/10.1016/j.powtec.2022.117521.
54. R.L. Coble: *J. Am. Ceram. Soc.*, 1958, vol. 41, pp. 55–62. https://doi.org/10.1111/j.1151-2916.1958.tb13519.x.
55. F. Nisar, J. Rojek, S. Nosewicz, K. Kaszyca, and M. Chmielewski: *Powder Technol.*, 2024. https://doi.org/10.1016/j.powtec.2024.119546.
56. F. Nisar, J. Rojek, S. Nosewicz, J. Szczepański, K. Kaszyca, and M. Chmielewski: *Comput. Part. Mech.*, 2024, vol. 11, pp. 2191–2201. https://doi.org/10.1007/s40571-024-00773-4.
57. F. Badry and K. Ahmed: *AIP Adv.*, 2020. https://doi.org/10.1063/5.0022375.
58. C. Chicone: *An Invitation to Applied Mathematics*, Academic, Amsterdam, 2017, pp. 703–18. https://doi.org/10.1016/B978-0-12-804153-6.50020-8.

59. C.E. Solivérez: The notion of electrical resistance, 2012. https://www.researchgate.net/publication/234037526.
60. J. Doumouro, E. Perros, A. Dodu, N. Rahbany, D. Leprat, V. Krachmalnicoff, R. Carminati, W. Poirier, and Y.D. Wilde: *Phys. Rev. Appl.*, 2021, vol. 15, p. 014063. https://doi.org/10.1103/PhysRevApplied.15.014063.